

國立臺灣大學理學院物理學系

碩士論文

Department of Physics

College of Science


National Taiwan University

Master Thesis

在 8 TeV 質心能量的質子對撞實驗中尋找頂夸克透過 Z 玻色子

及魅夸克（或上夸克）衰變的事件

Search for top decays through flavor changing neutral current  
process,  $t \rightarrow Z + q$ , in pp collisions at  $\sqrt{s} = 8 \text{ TeV}$

The logo of National Taiwan University is a circular seal. It features a central emblem with a bell and a book, surrounded by the university's name in Chinese characters: '國立臺灣大學' at the top and '愛·學·勵·品' at the bottom. The name '李昀翰' is written in the center of the seal.

李昀翰

Yun-Han Lee

指導教授：張寶棣 教授

Advisor: Pao-Ti Chang, Prof.

中華民國 102 年 6 月

June, 2013

國立臺灣大學碩士學位論文  
口試委員會審定書

論文中文題目

在質心能量為8 TeV的質子-質子對撞實驗中尋找頂夸克  
透過Z玻色子及魅夸克(或上夸克)衰變之事件

論文英文題目

Search for top decays through flavor-changing neutral current  
process,  $t \rightarrow Z + c (u)$ , in proton-proton collisions at  $\sqrt{s} = 8 \text{ TeV}$

本論文係 李昶翰 君 (R00222028) 在國立臺灣大學 物理 學系、  
所完成之碩士學位論文，於民國 2013 年 6 月 19 日 承下列考試委員  
審查通過及口試及格，特此證明

口試委員：

張寶棟

(簽名)

(指導教授)

陳凱凡

陳仲奇

侯維恩

鄭怡

## 摘要

在標準模型中，按照 GIM 機制的預測，以 Z 玻色子為媒介之跨世代衰變反應是被抑止的，在頂夸克的例子中，其反應率遠低於目前之測量範圍，但在其它模型中，該反應率可以目前之測量範圍。

我們使用了緊湊渺子線圈在 2012 年紀錄的質心能量為 8 TeV 之質子對撞數據，總通量約為  $19.5 \text{ fb}^{-1}$ ，以尋找頂夸克衰變至 Z 玻色子與魅夸克(或上夸克)的事件。

在大強子對撞機實驗中，大多數頂夸克係成對產生，故我們以  $t\bar{t} \rightarrow Wb + Zq$  之輕子性衰變為尋找標的，即 W 玻色子衰變至電子或渺子及對應的微中子，Z 玻色子衰變為電子或渺子對。我們使用了 b 簇射(jet)標記，以配對衰變至 Wb 的頂夸克，以反 b 簇射標記配對衰變至 Zq 的頂夸克。在此選擇條件下，背景之主要組成為  $Zt\bar{t}$  以及 WZ 反應。

我們以 b 簇射標記法進行數據導向之背景分析，預測將觀測  $3.08 \pm 0.85 \pm 0.76$  個背景事件，與蒙地卡羅法之預測一致。

在數據中僅觀察到一個滿足選擇條件的事件，符合標準模型之預測；我們計算出  $t \rightarrow Zq$  之衰變佔頂夸克衰變的百分率在 95% 之信心水準下不超過 0.06%。

關鍵詞：GIM 機制、大強子對撞機、緊湊渺子線圈、味變中性流、頂夸克

# Abstract

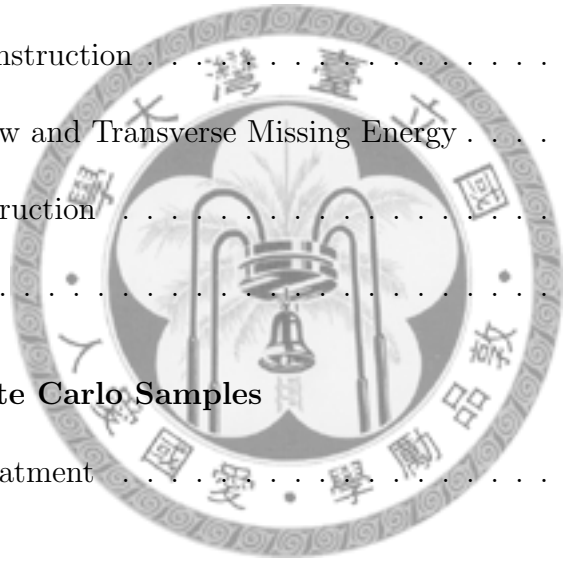
In the standard model, cross-generation interactions mediated by Z bosons, known as the flavor-changing neutral current (FCNC), are highly suppressed. For top quark FCNC decay, the cross-section is far below the experimental limit. However, other models predict much higher cross-sections, and some of them are even within reach. Therefore, using the data sample corresponding to an integrated luminosity of  $19.5 \text{ fb}^{-1}$  proton-proton collisions at a center-of-mass energy  $\sqrt{s} = 8 \text{ TeV}$ , collected with the CMS detector at the LHC, we performed the search with the decay chain  $t\bar{t}$  to  $Wb+Zq$ , where W decays to a charged lepton and a neutrino and Z decays to two charged leptons. The data-driven analysis using b-tagging method is performed with the estimated background being  $3.08 \pm 0.85$ , which is consistent with the estimation of Monte-Carlo method. One event is observed in the data which is consistent with the expected background, and the upper limit of the branching fraction for  $t \rightarrow Z+q$  is calculated as 0.06% at the 95% confidence level.

Key words: GIM mechanism, LHC, CMS, FCNC, top

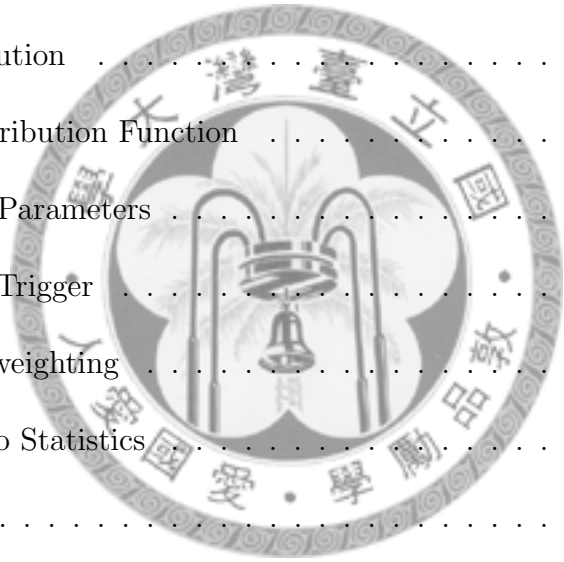
# Contents

<b>1</b>	<b>Introduction</b>	<b>13</b>
1.1	The Standard Model . . . . .	13
1.1.1	Quarks . . . . .	13
1.1.2	Leptons . . . . .	14
1.1.3	Gauge Bosons . . . . .	14
1.2	The Flavor-Changing Neutral Current of top decay . . . . .	16
1.2.1	The two-Higgs doublet models . . . . .	17
1.2.2	Supersymmetry models . . . . .	17
1.2.3	Technicolour model . . . . .	17
1.3	Proton-Proton Collisions . . . . .	17
1.4	Strategy . . . . .	18
<b>2</b>	<b>Experimental Apparatus</b>	<b>20</b>
2.1	The Large Hadron Collider . . . . .	20
2.2	The Compact Muon Solenoid . . . . .	21
2.2.1	Coordinate Conventions . . . . .	22
2.2.2	Magnet . . . . .	23
2.2.3	Inner Tracking System . . . . .	23

2.2.4	Muon System . . . . .	24
2.2.5	Electromagnetic Calorimeter . . . . .	25
2.2.6	Hadron Calorimeter . . . . .	26
2.2.7	Trigger System . . . . .	27
<b>3</b>	<b>Physical Object Reconstruction</b>	<b>29</b>
3.1	Track Reconstruction . . . . .	29
3.2	Vertex Reconstruction . . . . .	30
3.3	Electron Reconstruction . . . . .	31
3.4	Muon Reconstruction . . . . .	33
3.5	Particle Flow and Transverse Missing Energy . . . . .	34
3.6	Jet Reconstruction . . . . .	35
3.7	b tagging . . . . .	37
<b>4</b>	<b>Data and Monte Carlo Samples</b>	<b>39</b>
4.1	Pile-Up Treatment . . . . .	40
<b>5</b>	<b>Event Selection</b>	<b>44</b>
5.1	High Level Trigger . . . . .	45
5.2	Vertex Selection . . . . .	46
5.3	Electron Selection . . . . .	46
5.4	Muon Selection . . . . .	47
5.5	Jet Selection . . . . .	47
5.6	Z Selection . . . . .	49
5.7	MET and W Selection . . . . .	50
5.8	Top Selection . . . . .	50



<b>6</b>	<b>Background Analysis</b>	<b>54</b>
6.1	Data-Driven Method . . . . .	54
6.2	MC Analysis . . . . .	58
<b>7</b>	<b>Systematic Uncertainty</b>	<b>61</b>
7.1	Luminosity Measurement . . . . .	61
7.2	Cross Sections . . . . .	61
7.3	Lepton Isolation and Selections . . . . .	62
7.4	Jet Energy Scale and Jet Energy Resolution . . . . .	62
7.5	MET Resolution . . . . .	62
7.6	Parton Distribution Function . . . . .	63
7.7	MadGraph Parameters . . . . .	64
7.8	High Level Trigger . . . . .	64
7.9	Pile-Up Reweighting . . . . .	65
7.10	Monte Carlo Statistics . . . . .	66
7.11	b-tagging . . . . .	66
7.12	Systematic for Data-Driven background analysis . . . . .	66
<b>8</b>	<b>Summary</b>	<b>70</b>

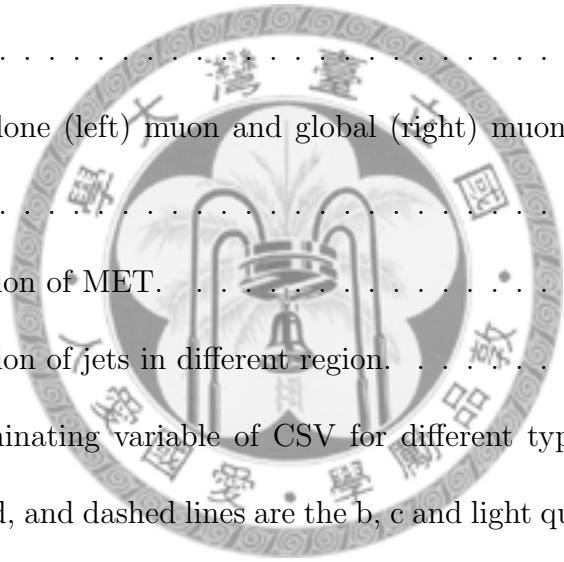


# List of Figures

1.1	A summary table of currently known elementary particles. The mass is labeled in natural unit. . . . .	15
1.2	The tree diagram (left) is suppressed in SM, while the loop diagram (right) is of very small cross section. . . . .	16
1.3	When proton (blue) collides to each other, hard interaction (red circles) and the underlying effect (pink dot) occurs. The resulting color particles, due to the color confinement, copiously creates more color particles (red and pink lines), and finally, all color particles binds together to form hadrons (green). . . . .	19
1.4	The gluon fusion is the main mechanism of top production in LHC experiment. . . . .	19
2.1	A plot showing the process of acceleration of protons. Four interaction points symboling different detectors are also shown in the plot, and the top one is the CMS detector. . . . .	21
2.2	The CMS detector. . . . .	22
2.3	The quarter view of the inner tracking system. . . . .	24
2.4	The quarter view of the muon chamber. . . . .	25
2.5	The quarter view of the ECAL crystals. . . . .	26



2.6	The quarter view of the ECAL, HCAL and the muon chamber. . . . .	27
2.7	The transverse view of CMS detector which summarize the methods for identifying different particles. . . . .	28
3.1	The resolution of $p_t$ and impact parameter of tracks. . . . .	30
3.2	The material budgets leads to energy loss of electrons. . . . .	31
3.3	Combining the ECAL and tracking information, a good resolution can be obtained in different $p_t$ region. . . . .	32
3.4	The standalone (left) muon and global (right) muon reconstruction efficiency. . . . .	33
3.5	The standalone (left) muon and global (right) muon reconstruction resolution. . . . .	34
3.6	The resolution of MET. . . . .	35
3.7	The resolution of jets in different region. . . . .	37
3.8	The discriminating variable of CSV for different types of jet. The solid, dotted, and dashed lines are the b, c and light quarks respectively. . . . .	38
4.1	An event after reconstruction. The green lines are the tracks of charged particles and the yellow dots are the vertices. . . . .	42
4.2	The pile-up distribution of the Run2012A data and the distribution assigned for MC production in 2012 summer. The division of these two gives the proper weights for different number of interaction. . . . .	42
5.1	The vertex DoF (left) and the number of vertex (right). . . . .	46
5.2	After Z selection, the $p_t$ (left) and $\eta$ (right) distributions of electrons. . . . .	47
5.3	After Z selection, the $p_t$ (left) and $\eta$ (right) distributions of muons. . . . .	48

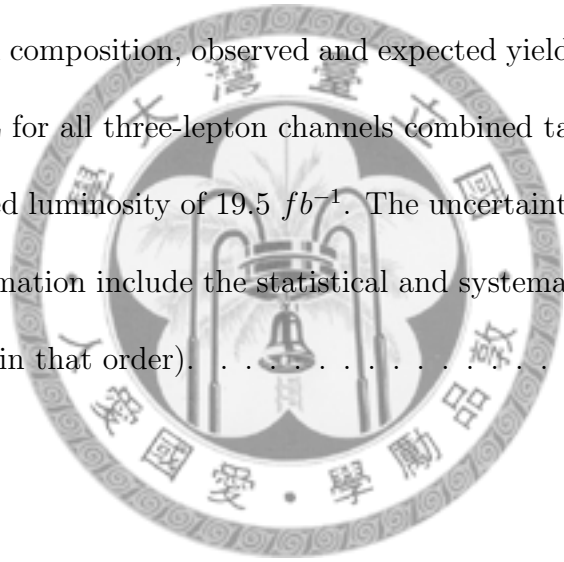


5.4	After Z selection, the pt (left) and eta (right) distributions of jets. . .	48
5.5	After Z selection, the pt (left) and mass (right) distributions of Z candidates in electron channel. . . . .	49
5.6	After Z selection, the pt (left) and mass (right) distributions of Z candidates in muon channel. . . . .	49
5.7	After Z and W selection, the W transverse mass (left) and the MET (right) distributions. . . . .	50
5.8	Before the mass window selection, the top Wb (left) and Zj (right) mass distributions. . . . .	51
5.9	The $\Delta\phi$ distribution of top pair. . . . .	52
5.10	The mass correlation distribution in data with the red dotted box labels the mass window. One sees that after applied all the selection, one event falls in the desired mass window. . . . .	52
6.1	The tree diagram showing the weight of each combination for a ttZ event. The acceptance is evaluated as 74% using ttbar MC sample. .	56
6.2	The toy study shows the sigma of $N_{BKG}$ is 0.85. . . . .	59
7.1	The $U_n$ to Z's pt (left) and $U_p$ to Z's pt (right) distributions. . . . .	63

# List of Tables

4.1	The data used in this analysis and the corresponding integrated luminosity. . . . .	41
4.2	The MC sample used in this analysis . . . . .	43
5.1	Summary of data yields after each cuts applied in sequential. . . . .	53
6.1	The combination considered for each process. Where $l$ can be $u$ , $d$ , $s$ quarks or gluon. Since four quarks are expected in $ttZ$ , further investigation considering jet acceptance is performed. . . . .	55
6.2	The probability for each combination to have exactly one $b$ -tagged. . . . .	57
6.3	The probability for each combination to have exactly zero $b$ -tagged. . . . .	58
6.4	The expected SM background contributions with $19.5 \text{ fb}^{-1}$ data. . . . .	60
7.1	Summary of uncertainties from MadGraph parameters. . . . .	65
7.2	The uncertainty of different sources for signal efficiency estimation. . . . .	67

7.3	The uncertainty of different sources for background estimation using data-driven method. The most significant source is b-tagging efficiency, which is estimated by varying the b-tagging efficiency by one sigma and re-construct the data-driven matrix. The second one is that from JES, JER and Pile-Up, which affect the top mass selection efficiency. . . . .	68
7.4	The uncertainty of different sources for background estimation using MC method. . . . .	69
8.1	Background composition, observed and expected yields, and limits at the 95% CL for all three-lepton channels combined tag selections for an integrated luminosity of $19.5 \text{ fb}^{-1}$ . The uncertainties in the background estimation include the statistical and systematic components separately (in that order). . . . .	71



# Chapter 1

## Introduction

### 1.1 The Standard Model

The Standard Model is a model developed to describe all known interactions between elementary particles: quarks, leptons and gauge bosons.

#### 1.1.1 Quarks

There are six quarks labeled by different flavors. They are categorized in three generations. The lightest quarks, up quark and down quark, forms the everyday particles like neutrons and protons. They form the first generation. In the end of 1947, the discovery of kaon leads to the idea of strange quark. As the energy scale grows in experiments, more heavy particles were found. The heaviest quark, which is the top quark found two decades ago, is almost 175 times the proton mass. Strange and charm quarks form the second generation; top and bottom quarks form the third generation. Quarks are fermions with spin  $\frac{1}{2}$ . The up, charm and top quarks carry charge  $+\frac{2}{3}$ ; the down, strange, and bottom quarks carry charge  $-\frac{1}{3}$ .

Each quark and gluon carry certain color, it can be blue, red or green (virtually). They obey the rule of color confinement, which states that the color particle cannot exist alone in the nature. Therefore, to form a colorless particle, it must be either formed by three quarks or a quark plus an anti-quark. The former is called a baryon and the later is called a meson. The collection of these two are called hadrons. The nature adapts the rule of baryon number conservation, which states that in a process, the number of baryon cannot change.

### 1.1.2 Leptons

There are six leptons labeled by their flavors. They can be separated by two categories: charged leptons, which are the electron, muon and tauon, carrying charge -1, and the neutrinos, which are the electron neutrino, muon neutrino and the tauon neutrino, being charge neutral. With their name they also form three generations. Different from quarks, leptons are colorless, so they are not involved in the strong interaction. Neutrinos are chargeless, so the only interaction for them is the weak interaction, which makes them hard to detect. Leptons obey the rule of lepton number conservation, which states that in any processes, the lepton number cannot change. The lepton number is defined as the number of leptons in certain generation; e.g., the electron and electron neutrino are of lepton number 1, and their anti-particles are of -1.

### 1.1.3 Gauge Bosons

The four gauge bosons are photon, gluon, Z and W. The former two are massless. The mass of Z boson is 91.2 GeV while the mass of W boson is 80.4 GeV. Only

gluon carries color, and only  $W$  carries charge, which can be  $+1$  or  $-1$ .

Photon is the mediator of electromagnetic interaction; particles of charge like quarks and charged leptons participate in this interaction. Gluon is the mediator of strong interaction, all quarks are involved in this interaction since all of them carry colors. The  $W$  and  $Z$  bosons are the mediators of weak interaction, which effect all particles. Since neutrinos carry neither color nor charge, they only participate in the weak interaction, thus making them hard to be detected.

Three Generations of Matter (Fermions)				
	I	II	III	
mass →	2.4 MeV	1.27 GeV	171.2 GeV	0
charge →	$\frac{2}{3}$	$\frac{2}{3}$	$\frac{2}{3}$	0
spin →	$\frac{1}{2}$	$\frac{1}{2}$	$\frac{1}{2}$	1
name →	<b>u</b> up	<b>c</b> charm	<b>t</b> top	<b>γ</b> photon
Quarks	4.8 MeV	104 MeV	4.2 GeV	0
	$-\frac{1}{3}$	$-\frac{1}{3}$	$-\frac{1}{3}$	0
	$\frac{1}{2}$	$\frac{1}{2}$	$\frac{1}{2}$	1
	<b>d</b> down	<b>s</b> strange	<b>b</b> bottom	<b>g</b> gluon
Leptons	<2.2 eV	<0.17 MeV	<15.5 MeV	91.2 GeV
	0	0	0	0
	$\frac{1}{2}$	$\frac{1}{2}$	$\frac{1}{2}$	1
	<b>ν<sub>e</sub></b> electron neutrino	<b>ν<sub>μ</sub></b> muon neutrino	<b>ν<sub>τ</sub></b> tau neutrino	<b>Z</b> weak force
	0.511 MeV	105.7 MeV	1.777 GeV	80.4 GeV
	-1	-1	-1	$\pm 1$
	$\frac{1}{2}$	$\frac{1}{2}$	$\frac{1}{2}$	1
	<b>e</b> electron	<b>μ</b> muon	<b>τ</b> tau	<b>W<sup>±</sup></b> weak force

Figure 1.1: A summary table of currently known elementary particles. The mass is labeled in natural unit.

## 1.2 The Flavor-Changing Neutral Current of top decay

The interaction mediated by a Z boson (or Higgs boson) is called the neutral current. In the Standard Model, if the quarks or leptons involved in the neutral current is of different flavor, the process will be suppressed. Such processes are called the flavor-changing neutral current.

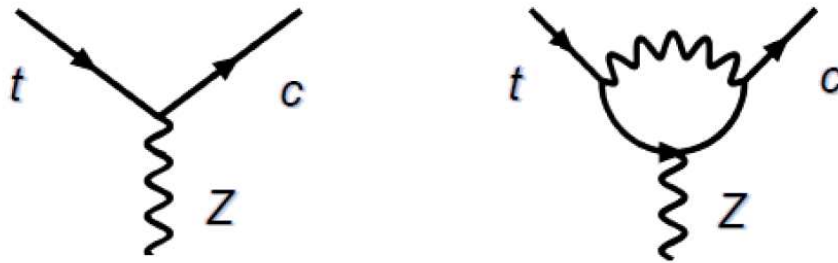


Figure 1.2: The tree diagram (left) is suppressed in SM, while the loop diagram (right) is of very small cross section.

In this analysis, we aim to search signal of the top quark decaying to Z and another light quark (charm or up). The tree level diagram is suppressed according to the GIM mechanism[1], and the loop diagram is of extremely small cross section. The branching ratio of this process is of the order of magnitude of  $10^{-14}$  as predicted by the Standard Model, which means the detection of this process can be a hint of new physics. Other models (referred to as extended or beyond SM, ESM or BSM) predict a higher branching ratio and some are possible to detect in LHC experiment. These models include the quark-singlet models[2], two-Higgs doublet models[3], R-violating Supersymmetry model, Technicolour model[4] and so on.



### 1.2.1 The two-Higgs doublet models

The two-Higgs doublet models predicts more than one Higgs boson and two of them are oppositely charged. These two oppositely charged Higgs boson provides a possible loop for the  $t \rightarrow Z + q$  process, and may have a branching ratio of the order of magnitude of  $10^{-6}$ .

### 1.2.2 Supersymmetry models

The supersymmetry models predicts a new symmetry in which every known fermion and boson is of a ‘super partner’ of different spin; i.e., for fermions, their partners are bosons, and for bosons, their partners are fermions. There are many different types of supersymmetry models, and the simplest one is called the minimal supersymmetric standard model. In this model, the R-parity is introduced. In the model which R-parity is violated, the  $t \rightarrow Z + q$  branching ratio can be as large as  $10^{-4}$ .

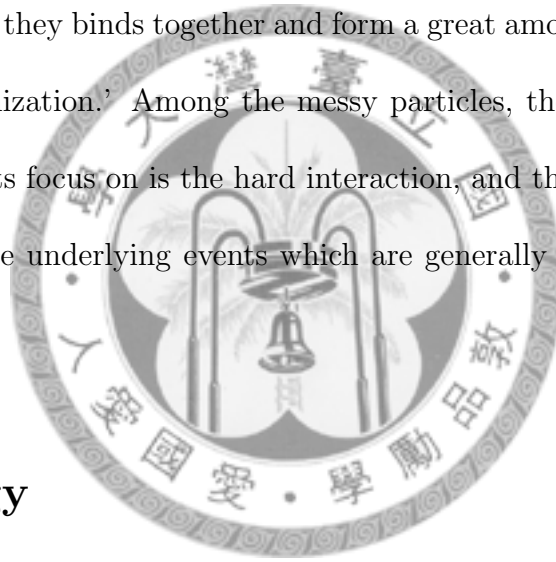
### 1.2.3 Technicolour model

In this model, a different particle (mechanism) is introduced in replace of the Higgs boson for the electroweak symmetry breaking issue. This model also provides explanation of the large top quark mass. The  $t \rightarrow Z + q$  branching ratio can be as large as  $10^{-5}$ .

## 1.3 Proton-Proton Collisions

It is said that the proton-proton collisions are like throwing trash cans together. It is because the protons are not elementary particles, it is composed of valence quarks,

two up and one down quarks, and of many gluons and sea quarks. When two proton collides with very high momentum transfer, often, we would expect a parton from one proton and another parton from the other proton interacts, which we call it hard interaction. The hard interaction may creates quarks, leptons, or gauge bosons; some are of color, and some are colorless. The rest part of the protons that did not participate the hard interaction sure are of color. With color confinement, these color particles quickly create many more color particles until they reach colorless state, this is what we refer to as ‘fragmentation.’ After the massive emergence of these color particles, they binds together and form a great amount of hadrons, which is called the ‘hadronization.’ Among the messy particles, the interesting one that most of the analysts focus on is the hard interaction, and those other interactions are referred to as the underlying events which are generally regarded as the noise contributor.



## 1.4 Strategy

The Large Hadron Collider provides events with the high energy collisions of protons, and therefore most of the top quarks are pair-produced through the gluon fusion. More than 99% of the top quark decays to b quark and W boson, so in our analysis, we search for one decaying to  $W+b$  and the other to  $Z+q$  in the full leptonic decay channels, where  $Z$  then decays to two electrons or muons and  $W$  decays to electron or muon with the corresponding neutrino. This channel is relatively clean since it consists of three leptons in the final state. However, the cleanness also makes the rare processes like  $ttZ$ ,  $tbZ$  non-negligible. The analysis steps will be provided in chapter five with more details.

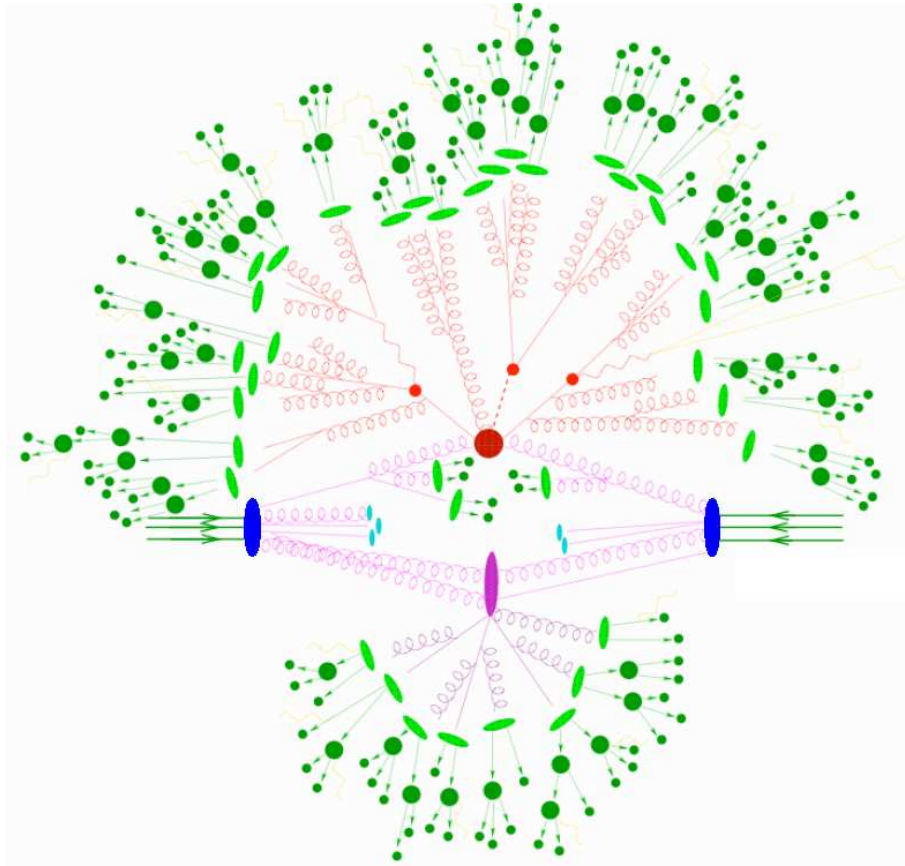


Figure 1.3: When proton (blue) collides to each other, hard interaction (red circles) and the underlying effect (pink dot) occurs. The resulting color particles, due to the color confinement, copiously creates more color particles (red and pink lines), and finally, all color particles binds together to form hadrons (green).

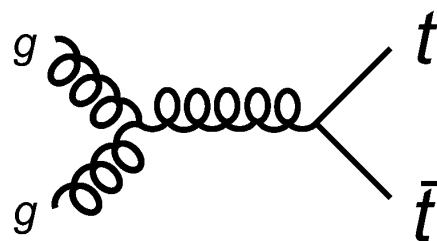


Figure 1.4: The gluon fusion is the main mechanism of top production in LHC experiment.

# Chapter 2

## Experimental Apparatus

This chapter provides the description for the apparatus, which includes the collider and the detector.[5]

### 2.1 The Large Hadron Collider

The Large Hadron Collider, short as LHC, is a proton-proton collider with designed  $\sqrt{s} = 14$  TeV. The acceleration is achieved in several steps: the proton bunches are first sent to the Linear accelerator to reach 50 MeV, followed by the Proton Synchrotron which raises the energy to 26 GeV. The beam is subsequently accelerated to 450 GeV in the Super Proton Synchrotron (SPS) and finally transferred to the LHC to reach the desired energy 7 TeV. On average, each bunch contains roughly  $10^{11}$  protons with bunch length being 7.55 cm and radius  $16.6 \mu\text{m}$ . To control the beam, superconducting magnets are exploited with a temperature of 1.9 K. The Radio-Frequency system works to accelerate the particles and compensates energy loss due to synchrotron radiation. In such a high energy proton-proton collision, the QCD processes give enormous background to the experiment. In addition, the

high luminosity makes the radiation damage become an important issue in detector development.

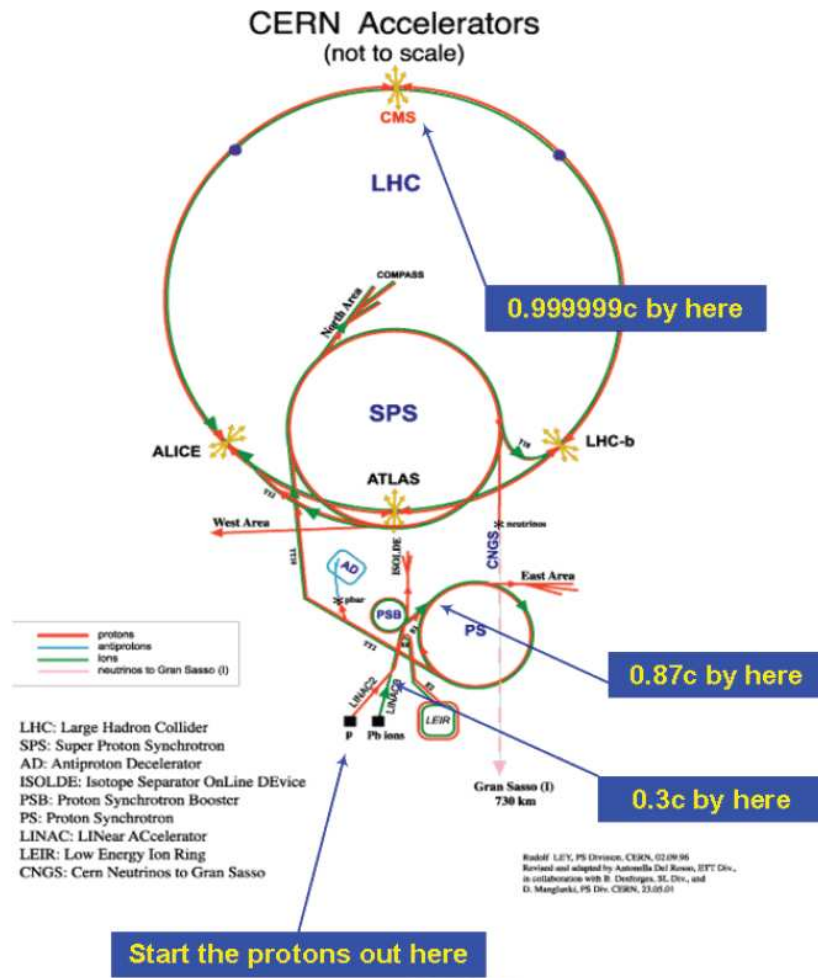


Figure 2.1: A plot showing the process of acceleration of protons. Four interaction points symboling different detectors are also shown in the plot, and the top one is the CMS detector.

## 2.2 The Compact Muon Solenoid

There are six experiments operating at the LHC. Two of them, which are the CMS, short for the Compact Muon Solenoid and ATLAS, short for A Toroidal LHC Appa-

ratuS, are aimed for the high pt physics. They search for the physics of and beyond the Standard Model. One of the major goal is to search for the long-predicted Standard Model Higgs, which, in July 2012, had already gave the world impressive results. The CMS detector is featured by its muon system as well as the inner tracking system, together they make CMS capable for fine measurements of the charged particles. Other main components are the electromagnetic calorimeter (ECAL), the hadronic calorimeter (HCAL), and the solenoid which provides 3.8 T magnetic field, through which the measurement of the momentum of charged particles can be made.

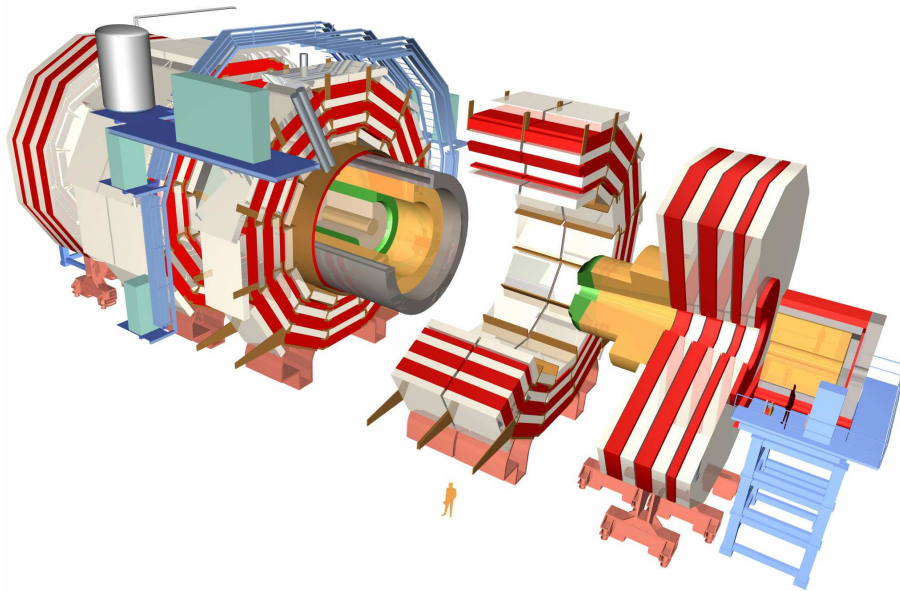


Figure 2.2: The CMS detector.

### 2.2.1 Coordinate Conventions

By convention, the nominal collision point is taken as the origin, with the y-axis pointing vertically upward, the x-axis pointing radially inward toward the center of the LHC and the z-axis pointing along the beam direction. The azimuthal angle is defined as the angle between the projection (on x-y plane) of the vector and the

x-axis. The polar angle is defined as the angle between the vector and the z-axis. The pseudo-rapidity is defined using the polar angle by  $\eta = -\ln \tan(\theta/2)$ . The cylindrical part of the detector is also referred to as the barrel, while the plates at the two ends are known as the endcaps.

### 2.2.2 Magnet

In the CMS detector, the magnetic field of 3.8 T is provided for the measurement of the momentum of charged particles. The high-purity aluminium-stabilised conductor and indirect cooling (by thermosyphon), together with full epoxy impregnation are used.

The overall conductor cross section is  $64 \times 22 \text{ mm}^2$ . The conductor was manufactured in twenty continuous lengths, each with a length of 2.65 km. Four lengths were wound to make each of the 5 coil modules.

### 2.2.3 Inner Tracking System

The tracking system using silicon sensors provides the measurements of the track and thus the momentum of charged particles. It consists mainly three regions. The detectors in the innermost region locates roughly 10 cm from the center cylindrically, the detectors here are also known as the pixel tracker due to their fine resolution. In the intermediate region where  $20 < r < 55 \text{ cm}$ , are another set of the detectors with less resolution. In the outermost region where  $r > 55 \text{ cm}$  lays the larger-pitch detectors. The later two are known as the strip tracker, and are called TIB (Tracker Inner Barrel) and TOB (Tracker Outer Barrel), respectively. The pixel detector consists of 3 barrel layers with 2 endcap disks on each side on them. The 3 barrel

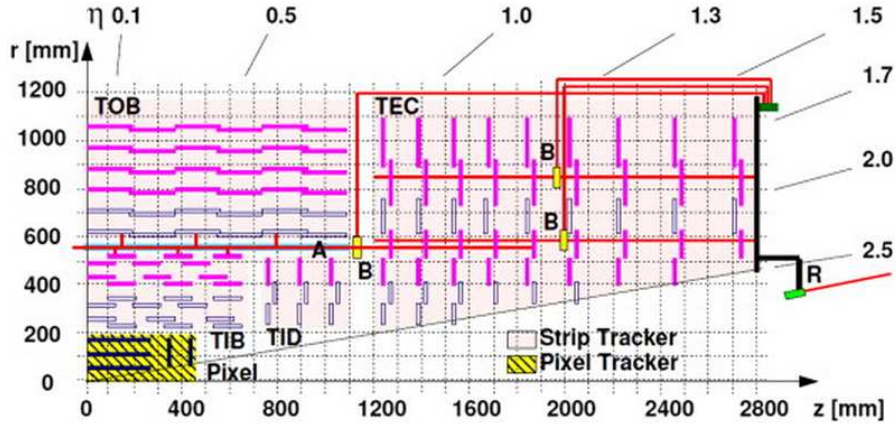


Figure 2.3: The quarter view of the inner tracking system.

layers are located at mean radii of 4.4 cm, 7.3 cm and 10.2 cm, and have a length of 53 cm. The second disks, extending from 6 to 15 cm in radius, are placed on each side at  $|z|=34.5$  cm and 46.5 cm. The spatial resolution of the pixel detector is about  $10 \mu\text{m}$  for the  $r\text{-}\phi$  measurement and about  $20 \mu\text{m}$  for the  $z$  measurement.

The TIB is made of 4 layers and covers up to  $|z| < 65$  cm while the TOD comprises 6 layers with a half-length of  $|z| < 110$  cm. The TEC (Tracker End Cap) and TID (Tracker Inner Disks) locate at the endcaps. Each TEC comprises 9 disks that extend into the region  $120 \text{ cm} < |z| < 280$  cm, and each TID comprises 3 small disks that fill the gap between the TIB and the TEC. Starting from inside, the resolution of these strip detectors vary from  $23\text{-}52 \mu\text{m}$  for the  $r\text{-}\phi$  measurement and  $230\text{-}530 \mu\text{m}$  for the  $z$  measurement.

## 2.2.4 Muon System

For the low momentum muon, the inner tracking system can provide good measurement; while for the high momentum ones the uncertainty become large due to the curvature being small. On contrary, the muon chamber locates in the outer region



can measure high momentum muons to a good precision while the low momentum ones, being scattered by the materials, cannot be well measured. Therefore, with both tracking system and muon chamber (full system), the capability of muon measurement of CMS is excellent. In muon chamber, three types of detectors are used: the drift tube, which covers the region  $|\eta| < 1.2$ , the cathode strip chambers, which covers the region  $|\eta| < 2.4$ , and the resistive plate chambers, which covers the region  $0.8 < |\eta| < 2.4$ . These detectors are chosen depending on the environment of the magnetic field and the radiation of their location.

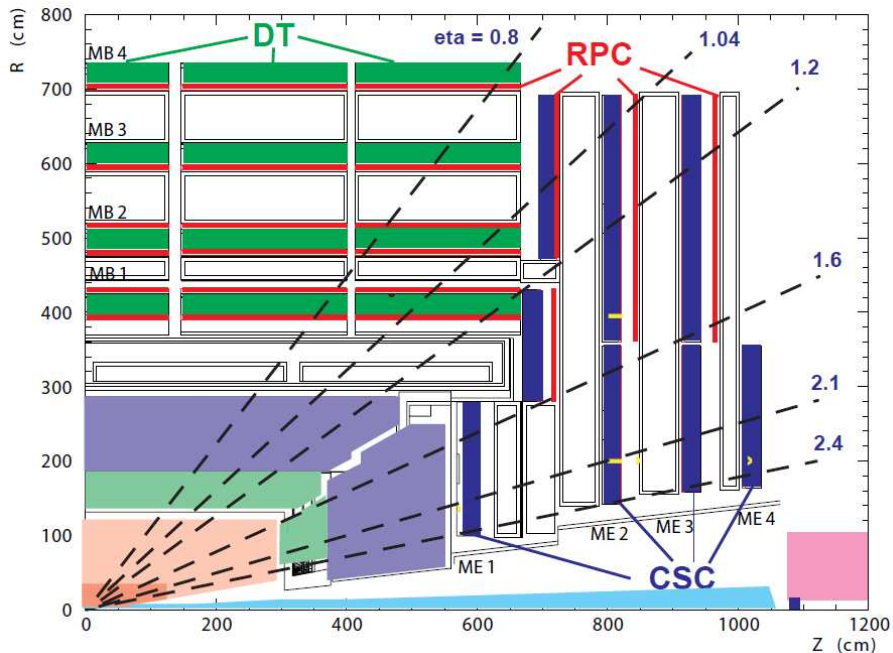


Figure 2.4: The quarter view of the muon chamber.

## 2.2.5 Electromagnetic Calorimeter

The electromagnetic calorimeter (ECAL) measures the energy of charged particles and photons. It is made of lead tungstate crystals with short radiation length (0.89 cm), fast response (80% of the light is emitted within 25 ns) as well as good radiation

resistance. The silicon avalanche photodiodes (APDs) and the vacuum phototriodes are used as photodetectors in the barrel and endcap region, respectively.

The ECAL in the barrel region, short as EB, covers the region of  $0 < |\eta| < 1.479$  with a total radiation length corresponding to  $25.8 X_0$ . The front face of the crystal in EB is about  $22 \times 22 \text{ mm}^2$ . The ECAL in the endcap region, short as EE, covers the region of  $1.479 < |\eta| < 3.0$ . They have a front face cross section of  $28.6 \times 28.6 \text{ mm}^2$  and a length of 220 mm ( $24.7 X_0$ ). Locating in front of EE, the preshower detector composed of silicon sensors aims to separate the photon of Higgs decay from those of pion decay.

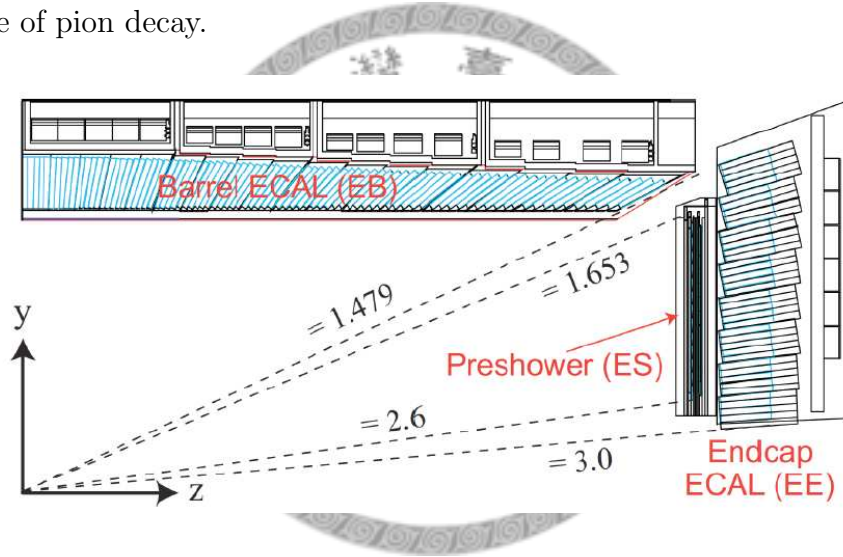


Figure 2.5: The quarter view of the ECAL crystals.

## 2.2.6 Hadron Calorimeter

The hadron calorimeter (HCAL) measures the energy of hadrons. It is made of brass which provides short interaction length and considerably small magnetic response. The plastic scintillator tiles read out with embedded wavelength-shifting (WLS) fibres are exploited.

The HCAL is separated into several regions: the barrel region, called HB, cov-

ering the pseudo-rapidity region  $-1.4 < \eta < 1.4$ , with segmentation  $\Delta\eta \times \Delta\phi = 0.087 \times 0.087$ , the outer region, called HO, covering the region  $-1.26 < \eta < 1.26$ , and the endcap region, called HE, which covers the region  $1.3 < |\eta| < 3.0$ . As for  $3.0 < |\eta| < 5.0$ , the stell/quartz fibre forward calorimeter (HF) is used, whose also provide the luminosity measurement.

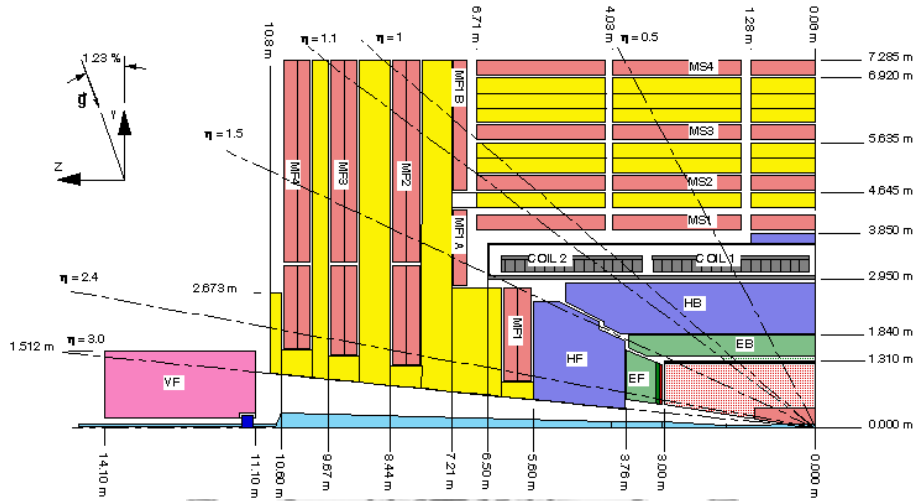


Figure 2.6: The quarter view of the ECAL, HCAL and the muon chamber.

## 2.2.7 Trigger System

Due to the high luminosity in the LHC, it becomes very important to have a mature trigger system. There are four major components in the CMS trigger system: the detector electronics, the Level-1 trigger processors (calorimeter, muon, and global), the readout network, and an online event filter system (processor farm) that executes the software for the High-Level Triggers (HLT).

The Level-1 trigger makes calculations in less than  $1 \mu s$ , while the time it takes for the transit is  $3.2 \mu s$ . A large fraction of events are discarded, only 1 crossing in 1000 is kept. When the Level-1 functioning, the high-resolution data is held in

pipelined memories. Commodity computer processors make subsequent decisions using more detailed information from all of the detectors in more and more sophisticated algorithms that approach the quality of final reconstruction. The ideal rate of L1 is 100 kHz. Afterwards, the data will be sent to the DAQ system with each event roughly 1.5 MB contained in hundreds of buffers. Then the processor runs the high-level trigger which reduce the rate to 100 Hz and then sends them to storage system. The separation of the L1 and HLT allows more flexible update for the HLT.

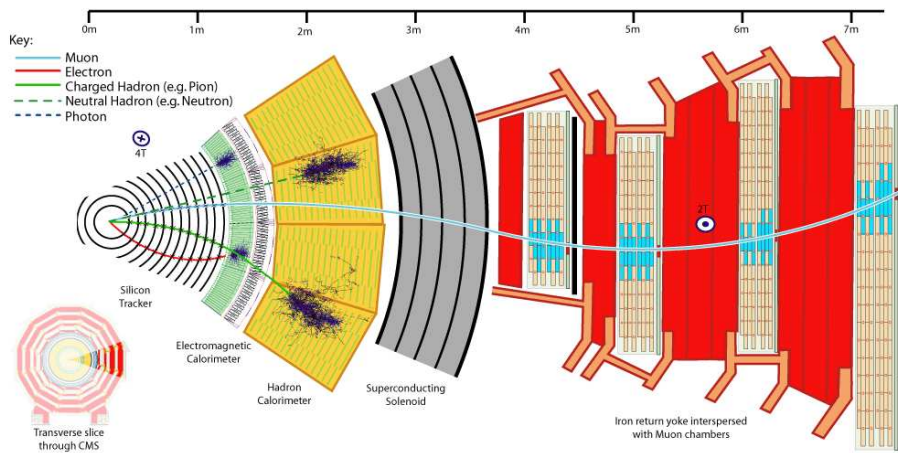


Figure 2.7: The transverse view of CMS detector which summarize the methods for identifying different particles.

## Chapter 3

# Physical Object Reconstruction

The physical objects used in this analysis include tracks, vertices, electrons, muons, the transverse missing energy and jets. The b-tagging algorithm is described as well.

### 3.1 Track Reconstruction

The connection of points of signals left on the tracking system gives tracks. The parameters of a track, which are the curvature, the impact parameter, the azimuthal angle, and the pseudo-rapidity, should be obtained in mainly three steps: seeding, building and fitting. The seed, which is the starting point, of track reconstruction, is the signal left on the pixel sensors. Due to the number of free parameters, at least two hits are required for deciding a track. Then, to build up the track, the outer layer is checked one by one to collect all the compatible hits and form track candidates. Finally, to avoid bias from the seeding constraints, an overall fitting is needed. The standard Kalman filter and smoother are used in this stage.

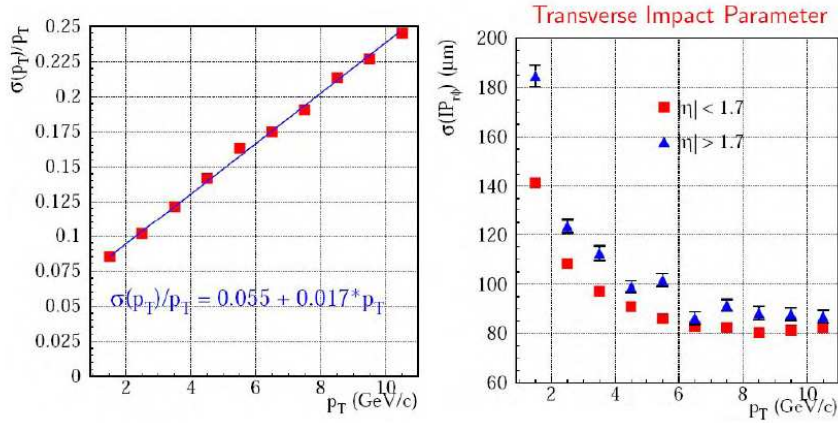


Figure 3.1: The resolution of  $p_T$  and impact parameter of tracks.

## 3.2 Vertex Reconstruction

The information of track can be used to obtain the vertex information. Vertex consists of the following free parameters: position, covariance matrix, and track parameters constrained by the vertex position and their covariances. The reconstruction of vertex is done through two steps: finding and fitting.

In the finding step, four sub-steps are involved: preselection, formation, fit, exclusion. First, the tracks with small impact parameter and  $p_T > 1.5$  GeV are chosen; then, clusters of tracks are formed according to their impact parameter along z-axis. Using these clusters, a fit is made to determine the vertex. What followed is the exclusion step where the bad fits are dropped. During the compatibility calculation, the Gaussian resolutions are assumed.

In the fitting step, the most often used algorithm is the Kalman filter (KVF). Mathematically, it is equivalent to a global least-squares minimization. This filter can also be used to improve estimation of the track momenta with constrains.

### 3.3 Electron Reconstruction

To reconstruct electrons, whose four-momentum should be decided, the information of tracking system and electromagnetic calorimeter (ECAL) is needed. The issue of energy loss is considered because of the materials in the tracking system. About 50% of the cases the electrons will radiate more than 50% of its energy before reaching ECAL. Another issue is that the electrons may come from the conversion of photons, which leads to the showering patterns.

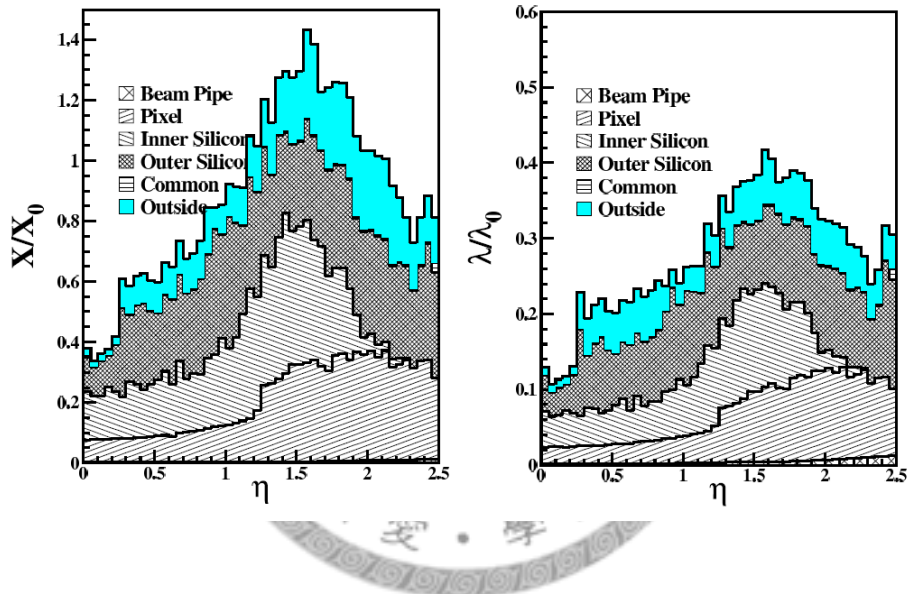


Figure 3.2: The material budgets leads to energy loss of electrons.

The steps can be separated to two parts: seeding and fitting. The seeding uses the information in the ECAL. ‘Hybrid’ and ‘island’ superclustering algorithms are used in determining the ECAL information in barrel and endcaps respectively. With a low threshold of the energy of supercluster, the efficiency of seeding can be as high as 99% for electrons with  $p_t$  higher than 7 GeV/c. The supercluster information will then be combined with the pixel detector to decide the two pixel hits needed for track finding.

The benefit of combining the information of ECAL and tracking system is based on the fact that the energy weighted average impact point of the electron and associated bremsstrahlung photons, as calculated using information from the supercluster in the ECAL, coincides (assuming a successful collection of photons) with the impact point that would have been measured for a non-radiating electron of the same initial momentum.

In the fitting stage, the problem of radiation energy loss made it important to have an improved tracking algorithm especially for those low pt electrons. The nonlinear Gaussian Sum Filter is thus introduced to make up the short coming of the Kalman filter. The average efficiency of the electron reconstruction is above 90%.

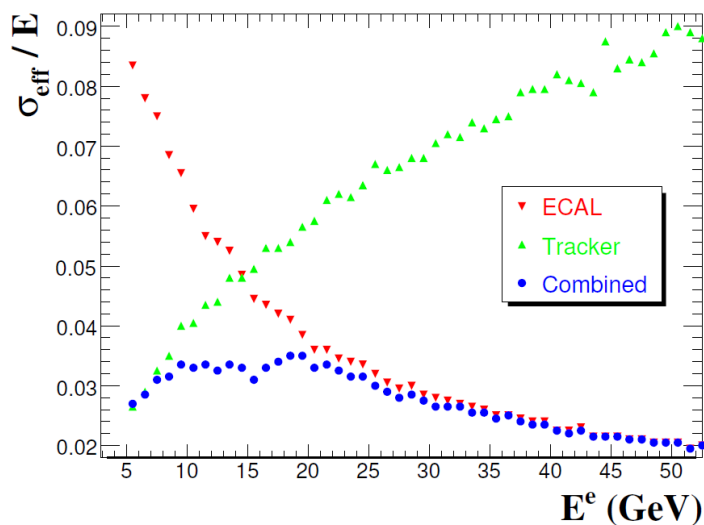


Figure 3.3: Combining the ECAL and tracking information, a good resolution can be obtained in different pt region.



### 3.4 Muon Reconstruction

The reconstruction of muon uses the information of muon system and the inner tracking system, and the step can be divided into local reconstruction, standalone reconstruction and global reconstruction.

The local reconstruction is done using the information of the CSC and DT detectors which decide the track segment for further reconstruction.

The standalone reconstruction uses only the information in the muon system. The track segment obtained in previous step will be combined with outer layer information using the Kalman-filter. Then a backward fit is performed to decide the vertex from which the muon comes.

In the final step, which is the global reconstruction, the inner tracking system information is exploited together with what was obtained in the standalone step. In this step, the muon track will be extrapolated to the tracking system and then the corresponding hits will be used to optimize the momentum measurement.

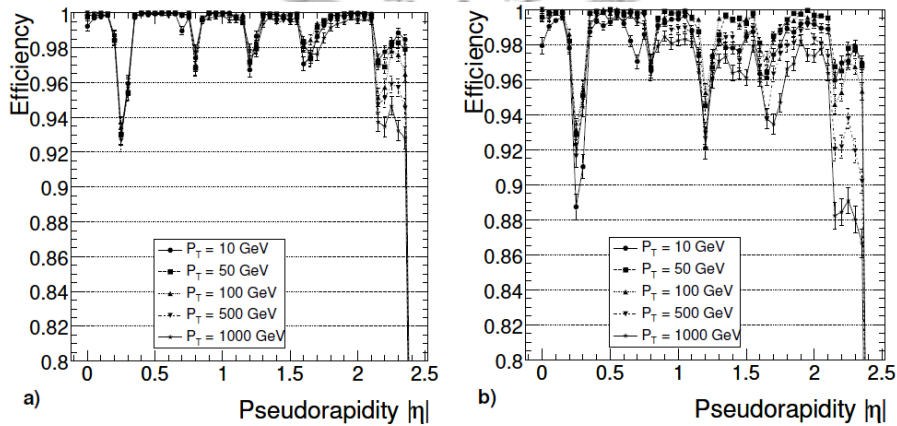


Figure 3.4: The standalone (left) muon and global (right) muon reconstruction efficiency.

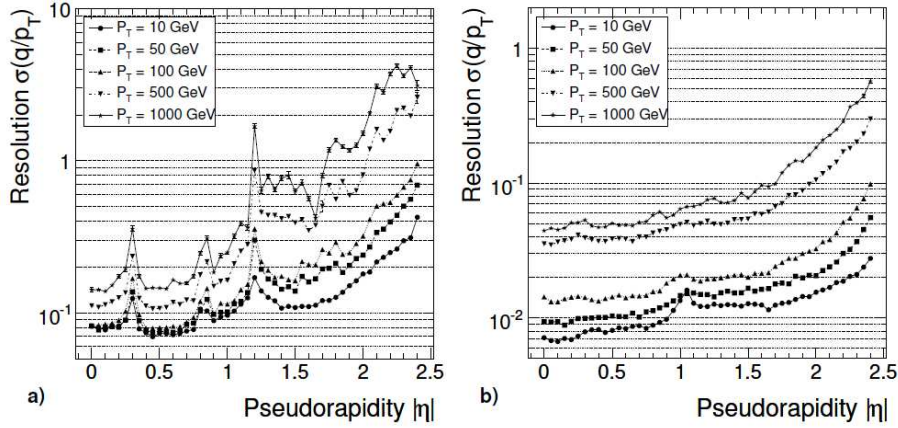


Figure 3.5: The standalone (left) muon and global (right) muon reconstruction resolution.

### 3.5 Particle Flow and Transverse Missing Energy

The particle flow is used during the reconstruction. It is based on the idea that one should include all detectors when doing the reconstruction of stable particles like electrons, muons, photons, hadrons (mainly pions and kaons). The list of particles will then be used to reconstruct jets as well as the transverse missing energy (short as MET).

The basic treatment is to use the tracks of charged particles and the clusters which is the energy left in the calorimeter as building blocks and reconstruct the particles as a whole.

Due to the well-functioning of the muon system, muons are first reconstructed and the corresponding blocks are removed from the list. What follows is the electron since it has little to do with the jet and MET reconstruction. Then the clusters and tracks related to the electrons are removed including those coming from the electron bremsstrahlung. The remaining tracks will be used to form charged hadrons candidates. What are left are the neutral particles with clusters energy deposit not

being able to match the track information. These are used to reconstruct the photon and the neutral hadrons. After all these one has filled a list of particles that may be used for the reconstruction of jets.

The MET the unbalanced energy on the transverse plane that coming from the neutrino or other weakly interacting particles created in the collision that cannot be detected. With the particle flow procedure, it is then straightforward to determine the MET: vector sum over all reconstructed particles in the event and then taking the opposite of this azimuthal, momentum two-vector.

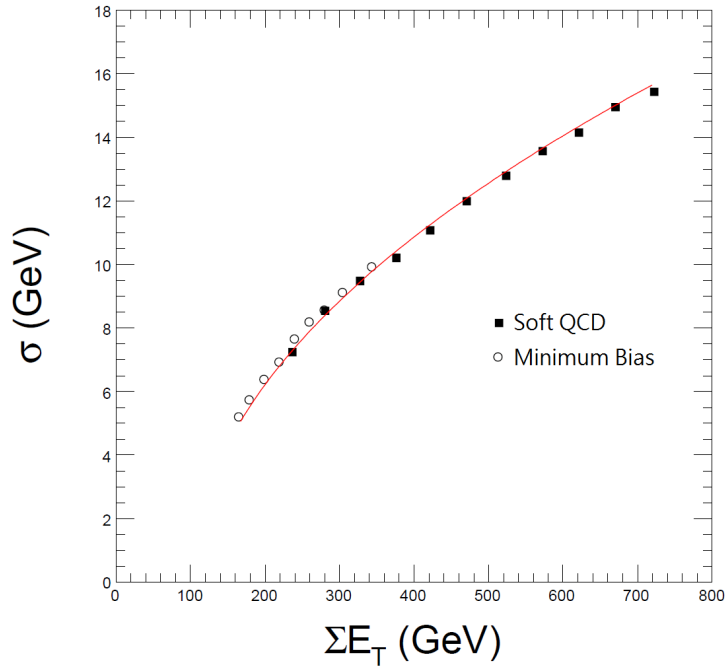


Figure 3.6: The resolution of MET.

## 3.6 Jet Reconstruction

In this analysis jets are referring to the product of the hadronization of the color particles; due to the color confinement, when a particle with color is created, it will

massively produce pairs of color particles until the color is balanced. These color particles will then form many hadrons and result in a jet signature. It is through clustering these hadronized particles that a jet is reconstructed.

There are many ways to do the clustering, and the algorithms frequently used are the  $k_T$ , Cambridge/Aachen and the anti- $k_T$  methods. The one used in this study is called anti- $k_t$  algorithm.

First, the distance variables are defined as:

$$d_{ij} = \min(k_{Ti}^{2p}, k_{Tj}^{2p}) \frac{\Delta_{ij}^2}{R^2},$$

where  $R$  is a parameter often set as 0.5.  $k_T$  is the transverse momentum, and the  $B$  indicates the beam.  $p$  is another parameter to be considered.

We collect all the possible candidates, either hadrons or the signal left in the calorimeter. Then this formula is applied to calculate the distance between two candidate  $i$  and  $j$ . If  $d_{ij}$  is larger than  $d_{iB}$ , then the two candidates are merged. Else, the candidate is preserved for other clustering.

The parameter  $p$  in the formula categorizes the methods. The  $p = 1$  case is the  $k_T$  method, the  $p = 0$  case is the Cambridge/Aachen method, and the  $p = -1$  is the anti- $k_T$  method.

The energy measured should be further corrected in the sense that there should be non-negligible loss of energy. The energy correction is done by several steps. The first step, called the Level 1 correction, is applied for the noise and pile-up suppression, and followed by the level two correction, which corrects the energy shift due to different  $\eta$  direction. And finally the level three correction corrects the pt to the ideal value when it is created[11].

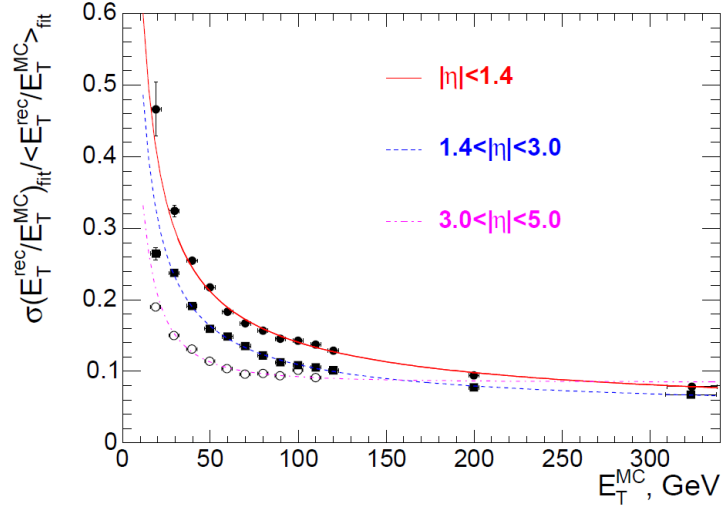


Figure 3.7: The resolution of jets in different region.

### 3.7 b tagging

In order to search the FCNC signal which contains one b quark in the pattern, the b-tagging technique is used for identifying if the jet is originated from a b quark (short as b jet).

This identification exploited the relatively long life time of b quark, which makes the vertex of a b jet shift from the primary vertex. Therefore, high spatial resolution track is of great importance.

In this analysis, the Combined Secondary Vertex method is used for b jet identification. First, the charged tracks in a jet are collected, and then the Trimmed Kalman Vertex Finder is exploited which selects the outliers of the tracks that can be used for secondary vertices reconstruction. Then the reconstructed secondary vertices' parameters and the tracks' parameters will be combined as a discriminating variable.

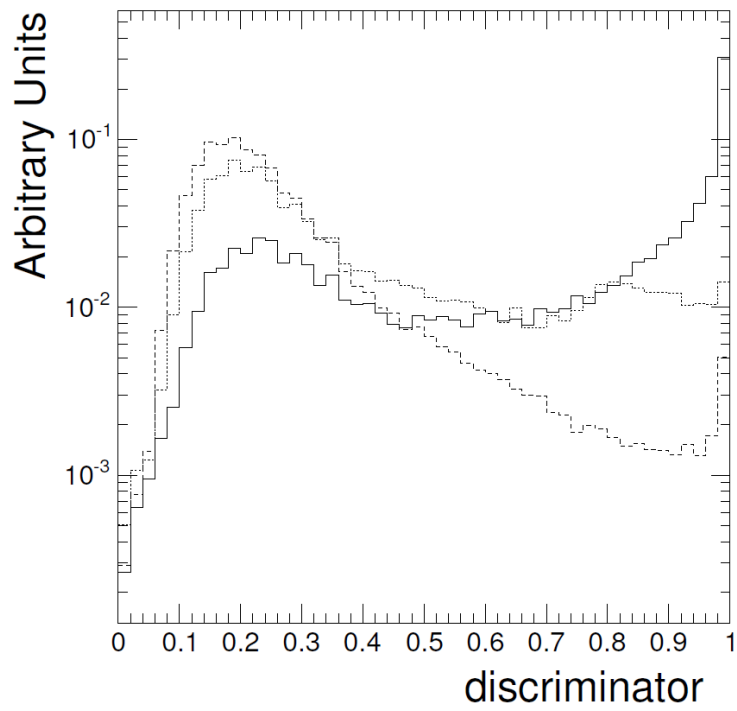
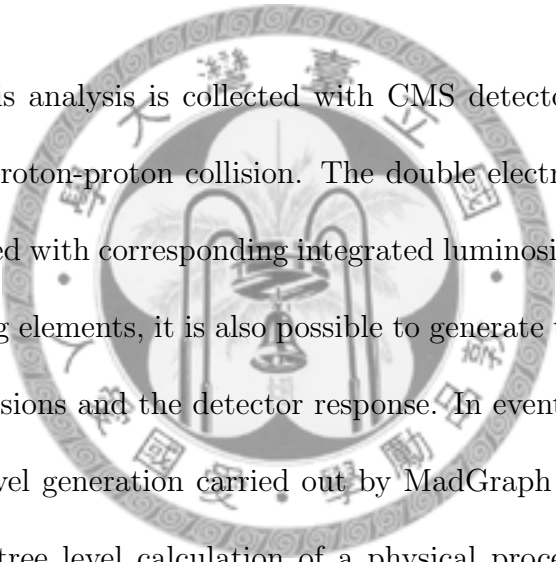


Figure 3.8: The discriminating variable of CSV for different types of jet. The solid, dotted, and dashed lines are the b, c and light quarks respectively.

# Chapter 4

## Data and Monte Carlo Samples



The data used in this analysis is collected with CMS detector from the LHC delivered 2012 8 TeV proton-proton collision. The double electron and double muon triggered data are used with corresponding integrated luminosity of  $19.5 \text{ fb}^{-1}$ . With the help of computing elements, it is also possible to generate the events which simulate the proton collisions and the detector response. In event generation, the first step is the parton level generation carried out by MadGraph 5[6] event generator, which performs the tree level calculation of a physical process using the helicity method[7]. Besides the process in standard model, MadGraph is also capable of doing calculation through a user-defined model. Then the output will be sent to PYTHIA 6[8] generator for the fragmentation and hadronization. TAUOLA[9] is also used for the emulation of tauon decay. The generated event will be sent to the GEANT 4 detector simulator which simulates the detector response. The first step is called generation, and the second step is called simulation. We refer to this sample as MC sample.

The MC sample is generated separately of different processes, while in data all

kinds of processes are mixed. Therefore, if we combine all the MC sample, it is possible that it can represent the result in data, and we can further estimate the fractions and distributions of different processes with different physical variables. Also, with MC sample we can determine the proper way to separate the signal process from the background and can have much higher statistics, for the event number in data is limited by the apparatus.

The FCNC MC signal MC sample contains the  $t\bar{t}b$  process where one of them decays to  $q$  (which may be  $c$ ,  $c\bar{c}$ ,  $u$  and  $u\bar{u}$ ) and  $Z$ , while the other decays to  $b$  (or  $b\bar{b}$ ) and  $W$ . Then the  $Z$  and  $W$  bosons decay to leptonic final states. Setting the branching ratio of this process to be 0.1%, we can then calculate the cross-section of this sample to be 0.047 pb. The sample contains equal amount of  $t$  to  $Zc$  and  $t$  to  $Zu$  events.

The other standard model background included in the study are the  $W$ ,  $Z$ ,  $WW$ ,  $WZ$ ,  $ZZ$ ,  $t\bar{t}b$ ,  $t\bar{t}bZ$ ,  $t\bar{t}bW$ , and single top. Among them, the major contribution comes from  $WZ$  and  $t\bar{t}bZ$  events which have very similar pattern comparing to FCNC in the desired final states. The table below summarize the sample used in this analysis.

## 4.1 Pile-Up Treatment

The LHC collisions are of extremely high luminosity. In 2012, there are often more than 20 interactions per event; although these events are of relatively small momentum transfer, the resulting energy deposit will be non-negligible. Therefore, on one hand, it is of great importance to model the pile-up effect in the MC simulation, while on the other hand, it is very crucial to reduce noise from pile-up effect.



Data	Int. Lumi. ( $pb^{-1}$ )
DoubleElectron(Muon)_Run2012A-13Jul2012-v1	808.47
DoubleElectron(Muon)_Run2012A-recover-06Aug2012-v1	82.14
DoubleElectron(Muon)_Run2012B-13Jul2012-v1	4428.67
DoubleElectron(Muon)_Run2012C-24Aug2012-v1	495.00
DoubleElectron(Muon)_Run2012C-PromptReco-v2	6401.67
DoubleElectron(Muon)_Run2012D-PromptReco-v1	7273.70
Total	19489.65

Table 4.1: The data used in this analysis and the corresponding integrated luminosity.

We use the number of interaction to describe the pile-up effect. For an event with high number of interaction, the pile-up is severe, while for an event with low number of interaction, the pile-up is not significant. The number of interaction is a probability function and in the 2012 Run period A, the most probable value is around 15. To model the pile up effect in the MC sample, the general approach is overlapping the low energy interactions several times with some shifts on the hard process. The probability function of the number of interaction varies with the luminosity; therefore, one first assign a probability function similar to but not exactly the same as the distribution in data. Then for those MC events with a certain number of interaction, it is reweighted with the probability ratio of data over MC of that number of interaction.

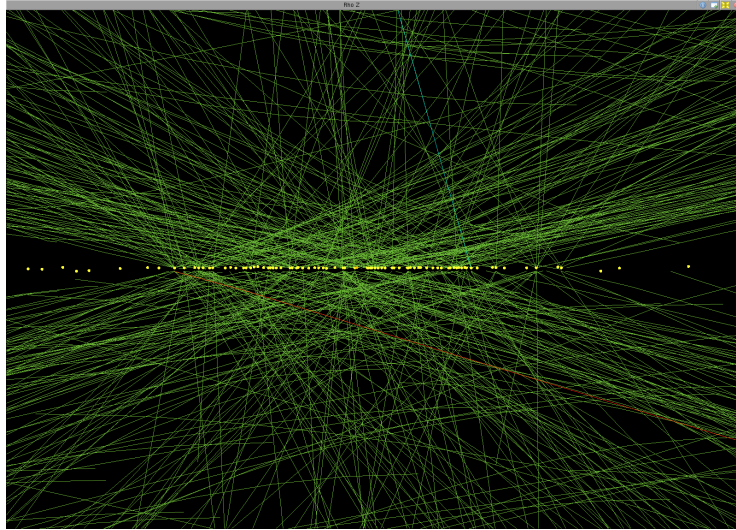


Figure 4.1: An event after reconstruction. The green lines are the tracks of charged particles and the yellow dots are the vertices.

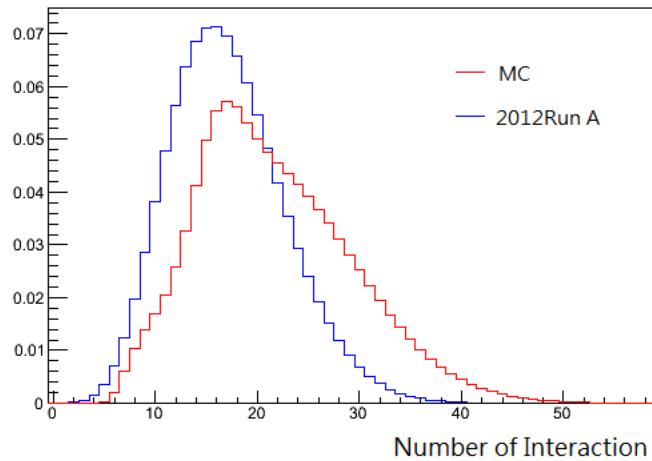
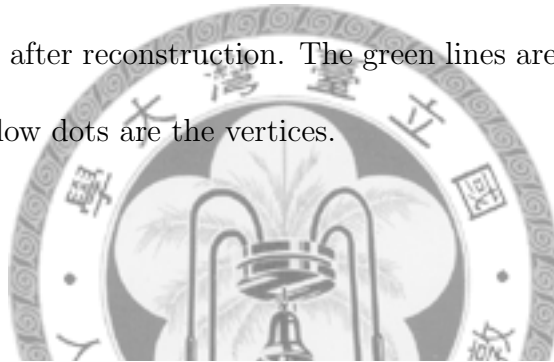


Figure 4.2: The pile-up distribution of the Run2012A data and the distribution assigned for MC production in 2012 summer. The division of these two gives the proper weights for different number of interaction.

Sample	Cross Section (pb)	Calculation Order
FCNC	0.047	assumed
TTJets	234	approx. NNLO
WJetsToLNu	37509	NNLO
DYJetsToLL	3503.7	NNLO
WWJetsTo2L2Nu	5.817	NLO
WZJetsTo2L2Q	2.467	NLO
WZJetsTo3LNu	1.189	NLO
ZZJetsTo2L2Nu	0.776	NLO
ZZJetsTo2L2Q	2.713	NLO
ZZJetsTo4L	0.213	NLO
T_s-channel	3.79	approx. NNLO
Tbar_s-channel	1.76	approx. NNLO
T_t-channel	56.4	approx. NNLO
Tbar_t-channel	30.7	approx. NNLO
T_tW-channel	11.1	approx. NNLO
Tbar_tW-channel	11.1	approx. NNLO
TTWJets	0.232	NLO
TTZJets	0.174	NLO
TBZToLL	0.0217	NLO

Table 4.2: The MC sample used in this analysis

# Chapter 5

## Event Selection

In this analysis, we look for the top pair events with one decaying to  $W+b$  and the other decay to  $Z+q$ , where  $q$  may be a charm or up quark, and  $W, Z$  decays to electrons or muons. Therefore, based on the decay channels of  $W$ , and  $Z$ , the search can be divided into four different channels:  $eee, ee\mu, e\mu\mu, \mu\mu\mu$ . The tauon channel is not considered due to the small reconstruction efficiency.

The event selection steps can be summarized as below:

1. Choose events that fire double electron or double muon high level trigger (HLT).
2. Select good vertex, electrons, muons, and jets.
3. Reconstruct  $Z$  candidate with two oppositely charged same flavor leptons.
4. Reconstruct  $W$  candidate with the addition charged lepton and MET confining  $W$ 's mass.
5. Veto events with more than three good leptons.
6. Veto events with less than two jets.

7. Choose events with exactly one b-tagged jet.
8. Reconstruct top pair, one using Z+q and the other using W+b.
9. Select the pair with maximum transverse open angle.
10. Select the top pair in the top mass window.

## 5.1 High Level Trigger

The high level trigger used in this study are

1. HLT\_Ele17\_CaloIdT\_CaloIsoVL\_TrkIdVL\_TrkIsoVL\_Ele8\_CaloIdT\_CaloIsoVL\_TrkIdVL\_TrkIsoVL
2. HLT\_Mu17\_TkMu8
3. HLT\_Mu17\_Mu8

These triggers select two leptons with one  $pt > 17$  GeV and the other  $pt > 8$  GeV as well as other calorimeter and tracker selection. For the double muon triggers, if either one fires or both, the event will be selected for further analysis. The further selection in the analysis are more tighter to avoid any effect from HLT.

These trigger efficiency, which is defined as the number of di-lepton events that pass our preliminary selections and also fire the trigger over the total number of di-lepton events that pass our preliminary selections, are measured to be 99%, 98%, 91% and 93% for  $eee$ ,  $ee\mu$ ,  $e\mu\mu$  and  $\mu\mu\mu$  channels, respectively. To prevent any bias from the trigger, we did this measurement by using the multi-jet triggered event which we assume to be non-relevant to lepton information. In these events, we look for events that has two same flavor leptons (electron or muon) that pass our lepton

and Z selections (the preliminary selections), then, the efficiency can be obtained by dividing the number of these events firing the di-lepton triggers over the total number of these events.

## 5.2 Vertex Selection

We assume the interaction to be the most prompt one in each triggered event; therefore, every candidates (leptons, jets) should be originated from the primary vertex which is the vertex of the highest track pt sum. They are required to have the fitting numbers of degrees-of-freedom (NDoF) greater than 4, the position  $|z| < 24$  cm and  $d_0 < 2$  cm (the transverse distance to the origin).

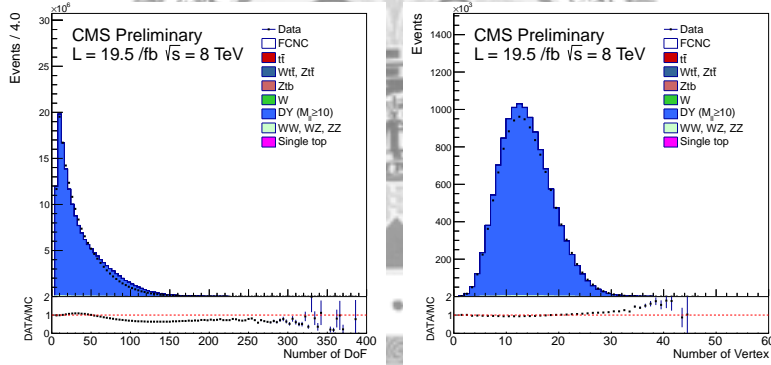


Figure 5.1: The vertex DoF (left) and the number of vertex (right).

## 5.3 Electron Selection

A good electron is selected with  $pt > 20$  GeV and  $|\eta| < 2.5$  and veto the gap region. Other variables are collected as a multi-variant-analysis variable called mva. We ask the mva variable to be larger than 0.5. The particle flow combined isolation requirement, which is defined as the energy sum of charged and neutral hadrons and

the photon over the  $p_T$  of the electron, is set as 0.15, within a cone of  $\Delta R = 0.3$ . In order to reduce extra energy sum from the pile-up effect, rho correction is applied.

Besides, the impact parameter on the transverse plane is required to be smaller than 0.04 cm, and should pass the ‘conversion veto’ requirement. The electrons with its  $\eta - \phi$  space too close to muons will be discarded.

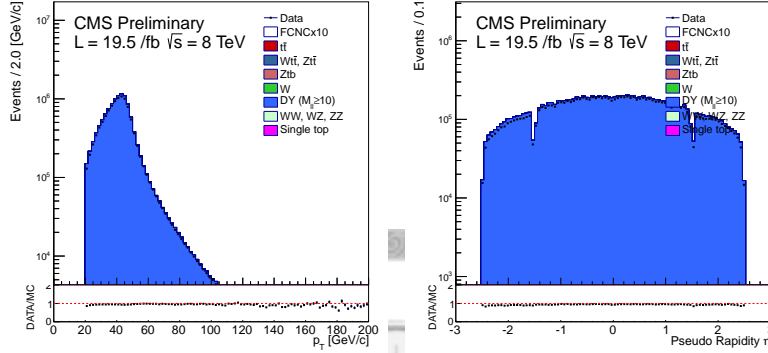


Figure 5.2: After Z selection, the  $p_T$  (left) and eta (right) distributions of electrons.

## 5.4 Muon Selection

A good muon is selected if it's a global muon with  $p_T > 20$  GeV and  $|\eta| < 2.5$ . The isolation is required to be smaller than 0.12 with a cone  $\Delta R = 0.4$ . Other selections include: valid tracker layers  $> 5$ ,  $d_{xy} < 0.2$ ,  $d_z < 0.5$ , global fitting  $\chi^2 < 10$ , valid pixel hit  $> 0$ , and matched muon station  $> 1$ .

## 5.5 Jet Selection

The anti- $k_T$  algorithm is used for jet reconstruction with  $\Delta R = 0.5$ . A good jet is selected with  $p_T > 30$  GeV and  $|\eta| < 2.4$ . Other jet identification is collected into a variable called ID, and the loose working point is used. Besides, the jets close

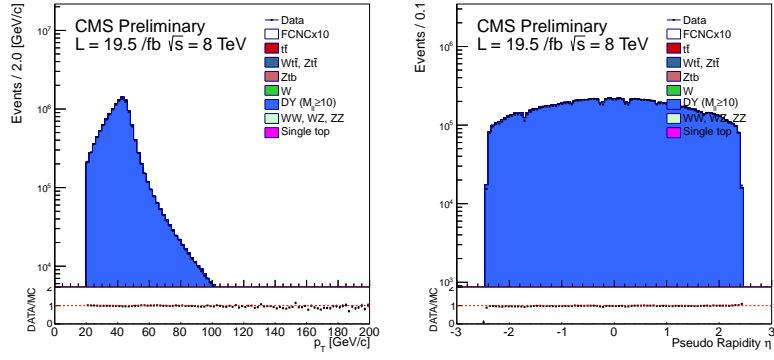


Figure 5.3: After Z selection, the  $p_t$  (left) and eta (right) distributions of muons.

to the leptons in its  $\eta - \phi$  space are discarded. For a b jet identification, the CSV algorithm is used and the medium working point, CSVM, is used. Events with more than one b-tagged jet or no b-tagged jet will be vetoed. The efficiency of CSVM is higher than 60%. The jet charged components which identified as originated from piled-up events are removed through the PFNoPU option in the standard PF2PAT sequence.

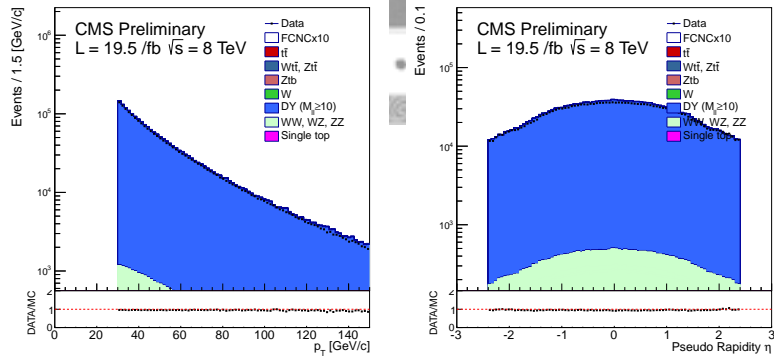


Figure 5.4: After Z selection, the  $p_t$  (left) and eta (right) distributions of jets.



## 5.6 Z Selection

A good Z candidate is reconstructed with two oppositely charged same flavor good leptons. The invariant mass of the two leptons should be within 78 to 102 GeV, and if there are more than one candidate exist, the closest one will be chosen.

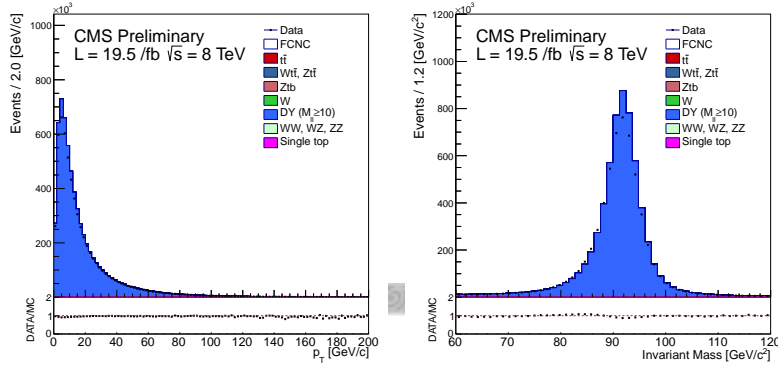


Figure 5.5: After Z selection, the pt (left) and mass (right) distributions of Z candidates in electron channel.

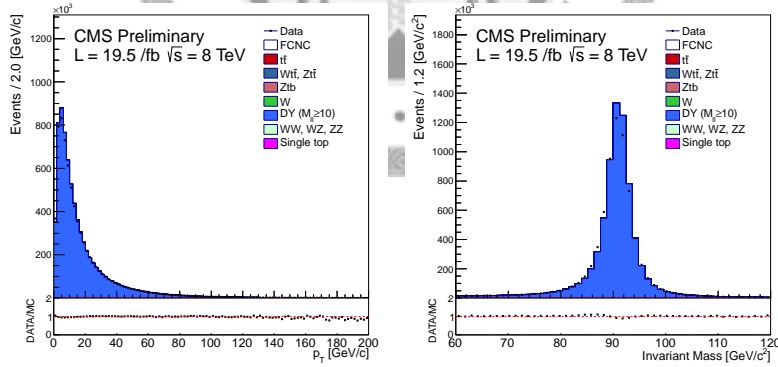


Figure 5.6: After Z selection, the pt (left) and mass (right) distributions of Z candidates in muon channel.

## 5.7 MET and W Selection

The MET is required to be larger than 30 GeV, and W is reconstructed with the third lepton other than those used in Z reconstruction. Since the  $p_z$  of the neutrino is unknown, only transverse mass of W can be obtained. To obtain a W candidate, the W nominal mass is assumed to be 80.3 and thus we can calculate the  $p_z$  of the neutrino by solving the equation below:

$$p_z = \frac{p_{zl}(p_{xl}p_{x\nu} + p_{yl}p_{y\nu} + M_W^2/2) \pm E_l \sqrt{(p_{xl}p_{x\nu} + p_{yl}p_{y\nu} + M_W^2/2)^2 - E_{T\nu}^2}}{E_l^2 - p_{zl}^2}$$

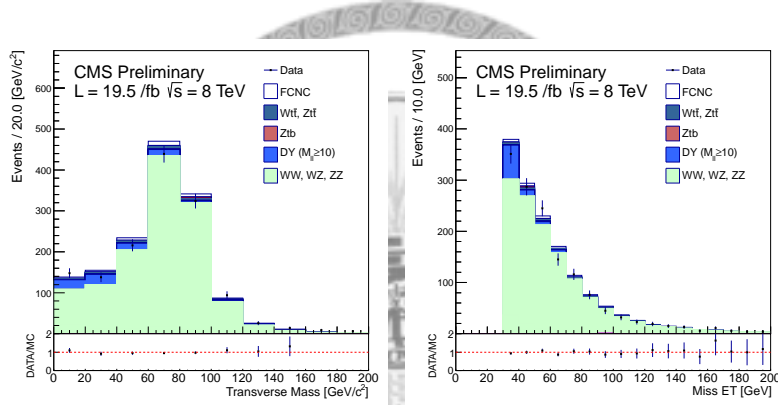


Figure 5.7: After Z and W selection, the W transverse mass (left) and the MET (right) distributions.

if there are more than one reasonable solutions, the larger one in its absolute value will be chosen. MC analysis shows that more than 60% of the times this is the right choice.

## 5.8 Top Selection

There are at most one b, Z and W candidate in each event, while there may be more than one light jet (non-b-tagged jet) candidate. Therefore, there is only one top

candidate reconstructed using  $W+b$ , while there may be more than one with  $Z+j$ . The pair that gives maximum  $\phi$  opening angle will be chosen. Then a top pair is selected, we further require the top from  $W+b$  should have invariant mass 137 to 207 GeV and the other one should be 147 to 197 GeV. If such an event is found, then it is taken as the FCNC candidate.

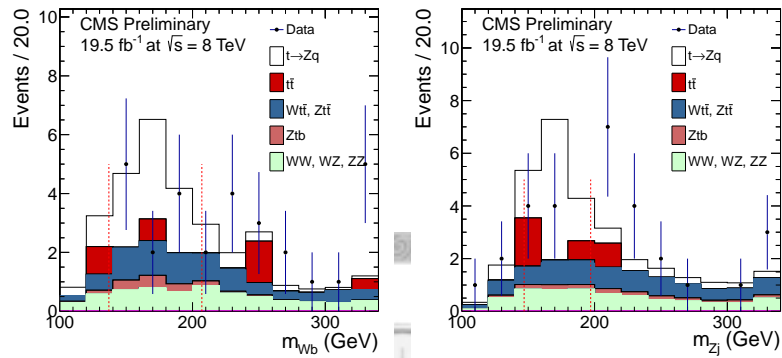


Figure 5.8: Before the mass window selection, the top  $Wb$  (left) and  $Zj$  (right) mass distributions.



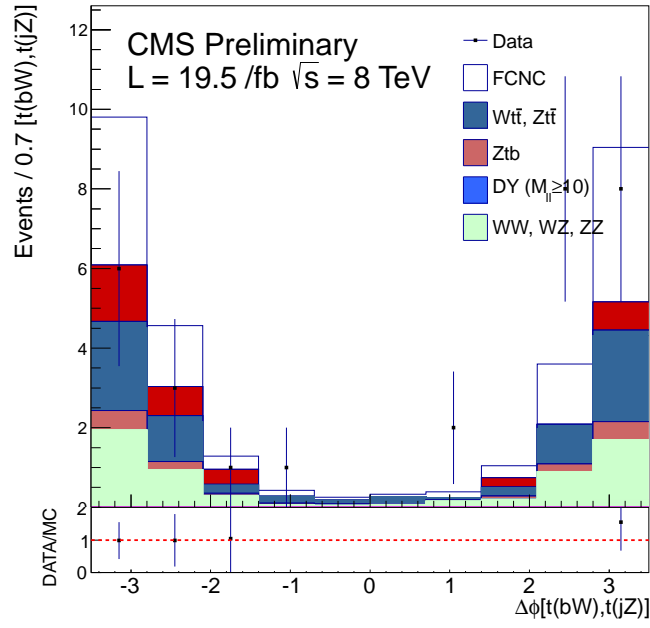


Figure 5.9: The  $\Delta\phi$  distribution of top pair.

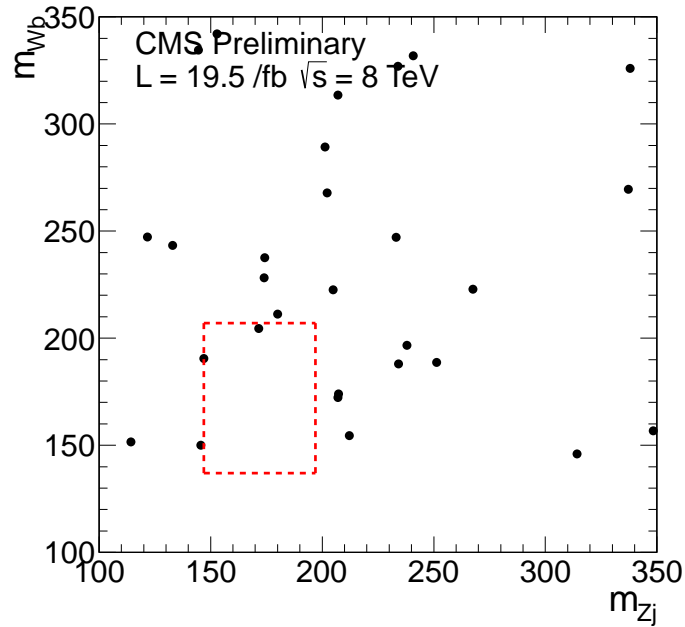


Figure 5.10: The mass correlation distribution in data with the red dotted box labels the mass window. One sees that after applied all the selection, one event falls in the desired mass window.

<i>e</i> channel	2012A	2012B	2012C-1	2012C-2	2012D
All	9469902	21325284	2582799	28582278	32131253
HLTrig. & Vertex	1154526	5847832	654472	8266121	6124273
2+ leptons	302112	1520527	170714	2163118	2403614
One <i>Z</i>	278701	1402333	157527	1993980	2216638
One <i>W</i>	50	303	27	352	435
MissET cut	23	154	17	203	247
2 Jets	6	29	6	36	30
1 <i>b</i> -tagged Jet	0	6	2	6	3
<i>t</i> Mass	0	0	0	0	0
$\mu$ channel	2012A	2012B	2012C-1	2012C-2	2012D
All	4729621	19948275	2054799	24333301	28485561
HLTrig & Vertex	1914787	14077704	1465706	16033682	17902238
2+ leptons	396089	2116989	236790	2997351	3415906
One <i>Z</i>	316911	1679549	188943	2376903	2689391
One <i>W</i>	72	286	31	461	543
MissET cut	36	154	16	244	322
2 Jets	6	19	3	35	37
1 <i>b</i> -tagged Jet	2	4	1	5	8
<i>t</i> Mass	0	0	0	1	0

Table 5.1: Summary of data yields after each cuts applied in sequential.

# Chapter 6

## Background Analysis

With the observed yield of the data and the estimated background yield, one may determine the branching ratio of FCNC. The background analysis is done with the data-driven method. In 2011, the method using lepton isolation information (see APPENDIX A) is exploited, and in 2012, we introduce another method which exploits the b-tagging information in the data. It is also compared with the MC analysis and the background estimation are consistent.

### 6.1 Data-Driven Method

The data-driven method is carried out by counting the number of events after good Z, W, and 2 jets selection ( $N_{all}$ ), the number of events that has exactly one b-tagged jet ( $N_{1tag}$ ), and the number of events with exactly zero b-tagged jet ( $N_{0tag}$ ). To this level, the dominant process are WZ ( $N_{0b}$ ), FCNC ( $N_{1b}$ ) and ttZ (or tbZ  $N_{2b}$ ). The WZ contains no b quark, the FCNC contains one b quark, and the ttZ contains two b quarks. We use the b-tagging efficiency and fake rate and thereby obtain the relationship between vector ( $N_{all}, N_{1tag}, N_{0tag}$ ) and vector ( $N_{0b}, N_{1b}, N_{2b}$ ). The

relation can be described as a matrix  $T$ .

$T$  is calculated in the following way:

Firstly, consider the weights of dominant jet combinations of each process, for example, the dominant jet combination is  $ll$  (two light quark) for  $WZ$ ; since it the only combination for  $WZ$ , it's weight is 1. For  $FCNC$  it's  $bl$  and  $bc$  can happen with equal rate, so the weights for  $bl$  and  $bc$  are both 0.5. For  $ttZ$ , it will be more complicated, and the jet acceptance is considered.

Sample	Assumed Combinations
$WZ$	$ll$
$FCNC$	half $bl$ , half $bc$
$ttZ$	half $bbcl$ , half $blll$
$tbZ$	$bb$

Table 6.1: The combination considered for each process. Where  $l$  can be  $u$ ,  $d$ ,  $s$  quarks or gluon. Since four quarks are expected in  $ttZ$ , further investigation considering jet acceptance is performed.

Secondly, one needs to consider the probability of each combination being tagged as 1 or 0 b jet. For example, for  $bc$  to be tagged as one b jet, the probability is  $\epsilon_b \times \epsilon'_c$ , and for it to be tagged as zero b jet, it is  $\epsilon'_b \times \epsilon'_c$ . Here  $\epsilon_b$  is defined as the b-tagging efficiency for a b jet,  $\epsilon_c$  is the b-tagging mis-tag rate for a c jet, and  $\epsilon_l$  is the b-tagging mis-tag rate for a light quark ( $u$ ,  $d$ ,  $s$ ,  $g$ ) jet. We label  $1 - \epsilon$  by  $\epsilon'$

Then combine the weight of each combination and the probabilities, one obtains

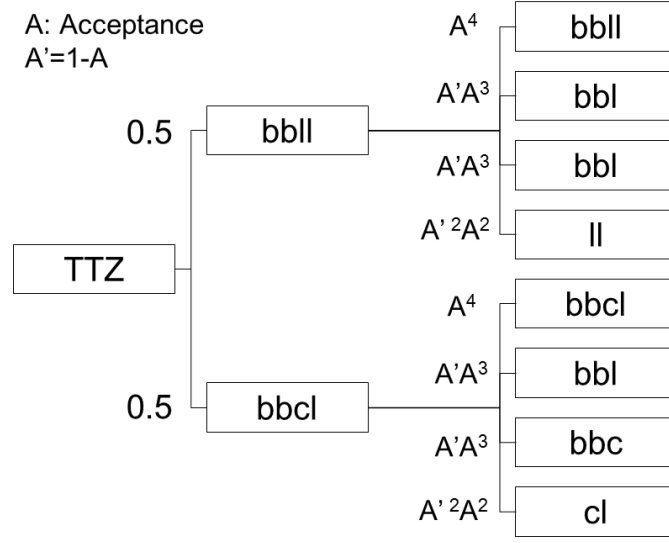


Figure 6.1: The tree diagram showing the weight of each combination for a ttZ event. The acceptance is evaluated as 74% using ttbar MC sample.

the proper matrix elements. Then we write the equation below:

$$\begin{pmatrix} N_{all} \\ N_{1tag} \\ N_{0tag} \end{pmatrix} = \begin{pmatrix} 1 & 1 & 1 \\ 0.085 & 0.58 & 0.47 \\ 0.91 & 0.36 & 0.21 \end{pmatrix} \begin{pmatrix} N_{0b} \\ N_{1b} \\ N_{2b} \end{pmatrix},$$

where  $(N_{all}, N_{1tag}, N_{0tag})=(207,37,161)$ . Then inverse the matrix:

$$\begin{pmatrix} 0.35 & -1.11 & 0.82 \\ -3.04 & 5.19 & 2.86 \\ 3.69 & -4.08 & -3.67 \end{pmatrix} \begin{pmatrix} N_{all} \\ N_{1tag} \\ N_{0tag} \end{pmatrix} = \begin{pmatrix} N_{0b} \\ N_{1b} \\ N_{2b} \end{pmatrix}$$

So we obtain the event number of the process with 0b (WZ), 1b (FCNC) and 2b (ttZ). The 0b and 2b processes are considered as our background events. They are 162.87 and 23.67 respectively.

To this step, the number of  $N_{0b}$  and  $N_{2b}$  are before the b-tagging selection as well as top mass selection.



Combination	Probability of 1 b-tagged
ll	$2\epsilon_l\epsilon'_l$
bl	$\epsilon_b\epsilon'_l + \epsilon'_b\epsilon_l$
bc	$\epsilon_b\epsilon'_c + \epsilon'_b\epsilon_c$
bb	$2\epsilon_b\epsilon'_b$
bbl	$2\epsilon_b\epsilon'_b\epsilon'_l + \epsilon'_b\epsilon'_b\epsilon_l$
bbc	$2\epsilon_b\epsilon'_b\epsilon'_c + \epsilon'_b\epsilon'_b\epsilon_c$
bbll	$2\epsilon_b\epsilon'_b\epsilon'_l\epsilon'_l + 2\epsilon'_b\epsilon'_b\epsilon_l\epsilon'_l$
bbcl	$2\epsilon_b\epsilon'_b\epsilon'_c\epsilon'_l + \epsilon'_b\epsilon'_b\epsilon'_c\epsilon_l + \epsilon'_b\epsilon'_b\epsilon_c\epsilon'_l$

Table 6.2: The probability for each combination to have exactly one b-tagged.

Therefore, we need to further multiply  $N_{0b}$  by matrix element  $T_{21}$  and  $N_{2b}$  by matrix element  $T_{23}$ , which are the probability of them to be tagged as a one b events.

$$N_{0b1tagged} = 162.87 \times 0.085 = 13.91,$$

$$N_{2b1tagged} = 23.67 \times 0.47 = 11.15$$

Then we multiply the top selection efficiency estimated by the MC analysis to reach the final number of background events.

$$N_{0bfinal} = 13.91 \times 0.10 = 1.38,$$

$$N_{2bfinal} = 11.15 \times 0.15 = 1.70$$

$$N_{BKG} = 1.38 + 1.70 = 3.08$$

Finally, we obtain the number of background.

The statistical uncertainty of this method is estimated by the toy Monte-Carlo.

Combination	Probability of 0 b-tagged
ll	$\epsilon'_l \epsilon'_l$
bl	$\epsilon'_b \epsilon'_l$
bc	$\epsilon'_b \epsilon'_c$
bb	$\epsilon'_b \epsilon'_b$
bbll	$\epsilon'_b \epsilon'_b \epsilon'_l \epsilon'_l$
bbc	$\epsilon'_b \epsilon'_b \epsilon'_c$
bbll	$\epsilon'_b \epsilon'_b \epsilon'_l \epsilon'_l$
bbcl	$\epsilon'_b \epsilon'_b \epsilon'_c \epsilon'_l$

Table 6.3: The probability for each combination to have exactly zero b-tagged.

We perform the toy study by assume Poisson distribution for  $N_{all}$ ,  $N_{1tag}$  and  $N_{htag}$  with mean values being the counted values, 207, 37 and 9, note that  $N_{htag}$  is the number of events with more than one b-tagged jet, and so we can have  $N_{0tag} = N_{all} - N_{1tag} - N_{htag}$ . We don't use  $N_{0tag}$  as Poisson, because it's relatively high in statistics and thus not close to Poisson distribution.

We generate 0.1 million toys of  $N_{all}$ ,  $N_{0tag}$  and  $N_{1tag}$  and do the calculation above. The standard deviation of the distribution of  $N_{BKG}$  is taken as the uncertainty. The uncertainty thus obtained is 0.85. This number is also cross-checked by the error propagation with consistent result.

## 6.2 MC Analysis

With MC Analysis, we estimated the background number to be  $3.19 \pm 0.72$  (stat.), which is consistent to the result of data-driven method. Most of the Standard

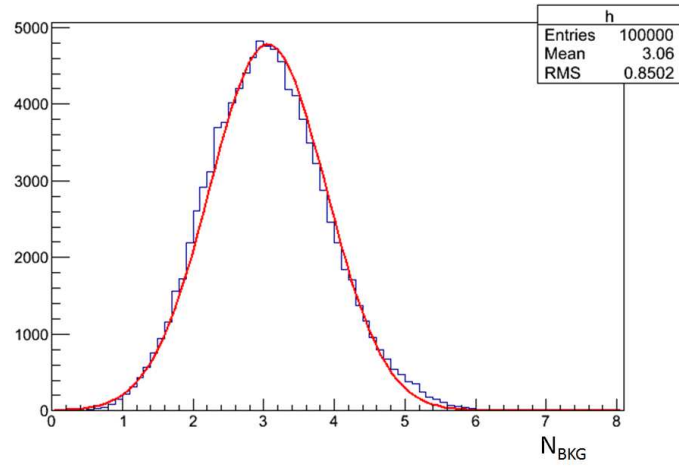
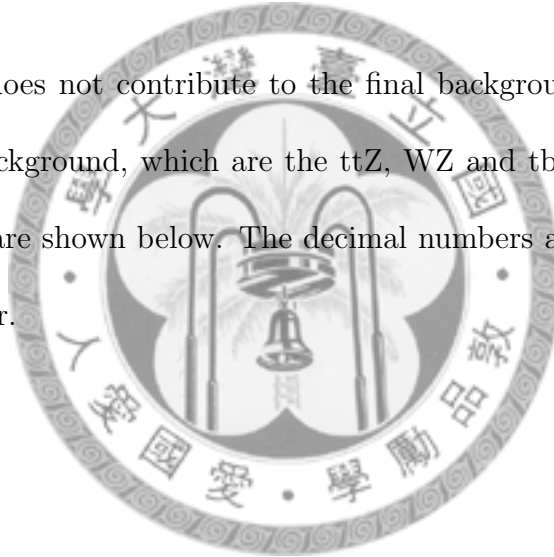


Figure 6.2: The toy study shows the sigma of  $N_{BKG}$  is 0.85.

Model background does not contribute to the final background yield, and for the signal and major background, which are the  $ttZ$ ,  $WZ$  and  $tbZ$ , the event numbers after each selection are shown below. The decimal numbers are because of the pile up reweighting factor.



Background	$\sigma \times \text{BR}$ (pb)	Processed	Seen	Events @ 19.5 /fb
$t\bar{t}$ Jets	234	6.8M	1.11	$0.74 \pm 0.48$
$W+$ Jets	37509	58.6M	0	0.0
$Z+$ Jets	3504	26.3M	0	0.0
$WW$	5.82	1.80M	0	0.00
$WZ3l$	1.09	2.03M	82.80	$0.87 \pm 0.10$
$ZZ4l$	0.18	4.86M	95.09	$0.07 \pm 0.01$
$t$ -S ch.	3.97	265K	0	0.0
$\bar{t}$ -S ch.	1.76	112K	0	0.0
$t$ -T ch.	56.4	3.5M	0	0.0
$\bar{t}$ -T ch.	30.7	1.9M	0	0.0
$tW$	11.1	496K	0	0.0
$\bar{t}W$	11.1	492K	0	0.0
$t\bar{t}W$	0.23	199K	3.97	$0.09 \pm 0.05$
$t\bar{t}Z$	0.17	214K	68.50	$1.09 \pm 0.13$
$tbZ$	0.0109	151K	234.8	$0.33 \pm 0.02$
Total:				$3.19 \pm 0.72$

Table 6.4: The expected SM background contributions with 19.5  $fb^{-1}$  data.

# Chapter 7

## Systematic Uncertainty

### 7.1 Luminosity Measurement

The luminosity measurement is done by using the pixel cluster information which is a function of number of interactions. The uncertainty from this measurement is considered in the upper limit calculation.

### 7.2 Cross Sections

The theoretical calculation of the cross sections come with uncertainties and are considered in the analysis. The electro-weak processes are of smaller uncertainties while the quark interaction can be of much larger uncertainties. This is used in MC analysis only.

## 7.3 Lepton Isolation and Selections

The lepton selection efficiency in MC is different from the one in data; therefore, a scaling factor is needed in MC events. This factor is obtained by using tag and probe technique to obtain the selection efficiency in data and in MC. The factor thus can be obtained by division, and the uncertainty is considered for the MC analysis.

## 7.4 Jet Energy Scale and Jet Energy Resolution

The energy of a jet is different from its originating quark, so a scaling factor is needed, and the uncertainty of this scaling is taken into account in our analysis. Besides, due to the relatively poor resolution in jets' energy, one vary the energy of jet by 10% of the jet resolution, where the jet resolution is defined as the energy difference between generated jet and the measured jet. The consequent difference in the overall selection efficiency is taken as the uncertainty.

## 7.5 MET Resolution

The MET is also an object of relatively poor resolution. The uncertainty of MET measurement is estimated using a Drell-Yan sample where there should in principle be no neutrino. The MET measured in this sample is considered as the uncertainty of MET resolution. The uncertainty is estimated in the following way: in an event, on the transverse plane, if some object  $U$  is created with the  $Z$  boson, then  $U$ ,  $Z$  boson and the MET should have zero vector sum. Therefore,  $U$ 's  $p_t$  can be decided with the MET and  $Z$  information. The  $U$ 's  $p_t$  can be separated into parallel ( $U_p$ ) to and normal ( $U_n$ ) to  $Z$ 's  $p_t$ . Ideally,  $U_p$  is the same as  $Z$ 's  $p_t$  and  $U_n$  is zero. The

deviation of ratio of ( $U_p$ ) to  $Z$ 's pt from one is taken as the uncertainty.

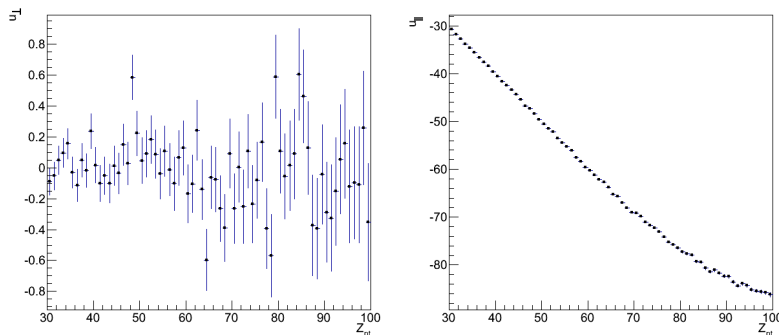


Figure 7.1: The  $U_n$  to  $Z$ 's pt (left) and  $U_p$  to  $Z$ 's pt (right) distributions.

## 7.6 Parton Distribution Function

Systematic uncertainties due to parton distribution functions (PDF) are traditionally estimated by using different PDF sets to generate the Monte Carlo samples and by taking the difference in cross sections observed with this procedure.

For the top FCNC signal MC samples, we estimate systematic uncertainties for different PDF tunes by a re-weighting method. The 44 parameter sets of CTEQ66 is used and the quadratic sum of deviations from the nominal case is quoted as the PDF uncertainty. Here we quote the deviations obtained with different error sets, which correspond to various theoretical uncertainties, as systematics due to the PDF choice. The estimated PDF uncertainty for FCNC top is about 7.0% while the weight uncertainty for background processes is about 5.4%.

For each parameter  $i = 1, \dots, 22$ , two values  $\sigma_i^\pm$  are extracted from the sum of

each event weights  $w_i^\pm$ , and the resulting uncertainties are calculated using:

$$\Delta\sigma^+ = \sum_{i=1\dots 22}^{\oplus} \max(\sigma_i^+ - \sigma_0, \sigma_i^- - \sigma_0, 0);$$

$$\Delta\sigma^- = \sum_{i=1\dots 22}^{\oplus} \max(\sigma_0 - \sigma_i^+, \sigma_0 - \sigma_i^-, 0).$$

This means that the full positive uncertainty to the cross section is taken to be the quadratic sum of all the positive shifts found for each PDF set (using the largest of the two in the case both  $w_i^+$  and  $w_i^-$  result in a positive shift), and the same is done for the negative uncertainty. The larger value between  $\Delta\sigma^+$  and  $\Delta\sigma^-$  is used when calculating the total systematic uncertainty.

## 7.7 MadGraph Parameters

The MC generator used in the study is MagGraph. The uncertainty from the generation is measured through varying the major input parameters. The mass of top, Q and the xqcut used in jet matching are varied and the corresponding change in the selection efficiency is taken as the uncertainty. This uncertainty is only used for signal efficiency estimation.

## 7.8 High Level Trigger

The efficiencies of high level triggers are different in data and in MC, and thus a factor should be applied in MC. Since we will find a good Z candidate in our selection, we estimate the efficiencies by looking for events with a good Z found. In MC, in DY sample where a good Z is found, we can calculate the rate that these



Table 7.1: Summary of uncertainties from MadGraph parameters.

Parameter	Uncertainty (%)
Top Mass -2 GeV	-4.1
Top Mass +2 GeV	1.4
Match $Q > 30$	-4.1
Match $Q > 60$	-3.9
$Q^2$ 4×	7.8
$Q^2$ 1/4	8.8
<b>Total uncertainty</b>	<b>13.8</b>

events fire the triggers. In data, to avoid bias, we use the multi-jet triggered events and calculate the rate. Then we compare and find the factor for MC, which also contains the uncertainty.

## 7.9 Pile-Up Reweighting

The number of interaction has different distributions in data and in MC. In MC, the distribution of number of interaction is described by a function called PU\_S10. In data, the distribution is obtained by measurements using the pixel and front-end calorimeter. The ratio is used on the MC for corresponding number of interaction. When calculating the number of interaction in data, the minimum bias event cross-section is used as an input parameter and we vary this parameter by 5% to see the difference in selection efficiencies.

## 7.10 Monte Carlo Statistics

Due to the limited event number and relatively clean channel, the statistics of MC become one of the important uncertainty source. This uncertainty is estimated assuming Poisson fluctuations of the final event number after all selections.

## 7.11 b-tagging

The b-tagging efficiency in MC is different from the one in data; therefore, a scaling factor is needed in MC events. This factor is obtained by study the  $t\bar{t}$  events to obtain the selection efficiency in data and in MC. The factor thus can be obtained by division, and the uncertainty is considered for the MC analysis.

## 7.12 Systematic for Data-Driven background analysis

For the systematic study of data-driven, we have to consider two different parts: those affect the matrix construction, and those affect the top mass selection efficiency. For the matrix, the main uncertainty comes from the b-tagging efficiency, which we vary the efficiency (mis-tag rate) by one sigma and re-do the data-driven calculation, then quote the change in the final background event number as the uncertainty. The other minor source is from that, when construct the matrix, we have to assume the jet component for the  $N_{Vt}$  being of half  $b\bar{b}c$  and  $b\bar{b}l$  (which means two b jets, one c jet and one light jet, and two b jets and two light jets, respectively.) We evaluate the effect of changing it from half half to 1:2 and 2:1.

For the top mass selection efficiency, since it's evaluated from MC, we consider the various sources: the jet energy scale, jet energy resolution and pile-up reweighting. For the lepton selection and high level trigger, we quote the max possible number. The total systematic uncertainty of data-driven method is 25%.

Source	Uncertainty (%)
Trigger efficiency	5
Parton distribution functions	7
Lepton selection	6
Pileup events	3
Top quark mass	4
Matching threshold	6
$Q^2$	12
MET resolution	3
Cross section	7
b tagging	5
JES	4
Total	19

Table 7.2: The uncertainty of different sources for signal efficiency estimation.

Table 7.3: The uncertainty of different sources for background estimation using data-driven method. The most significant source is b-tagging efficiency, which is estimated by varying the b-tagging efficiency by one sigma and re-construct the data-driven matrix. The second one is that from JES, JER and Pile-Up, which affect the top mass selection efficiency.

Source	total (%)
JES & JER (MET)& PU	14
MC Stat.	5
$N_{Vtt}$ component	3
$b$ -tagging	18
<b>Systematic uncertainty</b>	<b>23</b>

Table 7.4: The uncertainty of different sources for background estimation using MC method.

Source	total (%)
Cross section	38
HLT	5
Lepton	6
JES & JER (MET)	11
MET resolution	3
Parton Dist. func.	36
MC Stat.	32
Pile-up re-weight	7
$b$ -tagging	7
<b>Systematic uncertainty</b>	<b>64</b>

# Chapter 8

## Summary

With data-driven method, the estimated background is  $3.08 \pm 0.85 \pm 0.76$ . With MC analysis, we expect  $3.19 \pm 0.72 \pm 2.03$  SM background events.

The former one leads to an expected upper limit of  $\mathcal{B}(t \rightarrow cZ)$  to be less than 0.09%. The corresponding  $1\text{-}\sigma$  and  $2\text{-}\sigma$  bounds are [0.06%, 0.13%] and [0.05%, 0.20%], respectively. With one events surviving the full selection. This corresponding to an U.L. of  $\mathcal{B}(t \rightarrow cZ) < 0.06\%$  considering the systematical uncertainties on both signal efficiency and background contribution.

Selection	Data-driven Estimation	SM MC Prediction
WZ		$0.87 \pm 0.10 \pm 0.30$
ZZ	$1.38 \pm 0.06 \pm 0.40$	$0.07 \pm 0.01 \pm 0.03$
Drell-Yan		$0.00 \pm 0.03 \pm 0.02$
$t\bar{t}$		$0.74 \pm 0.70 \pm 1.16$
$Zt\bar{t}$	$1.70 \pm 0.85 \pm 0.65$	$1.09 \pm 0.13 \pm 0.77$
$Wt\bar{t}$		$0.09 \pm 0.05 \pm 0.11$
$Ztb$		$0.33 \pm 0.02 \pm 0.20$
Total background	$3.08 \pm 0.85 \pm 0.76$	$3.19 \pm 0.72 \pm 2.03$
Observed events	1	—
Expected limit	0.09%	0.10%
Observed limit	0.06%	0.06%

Table 8.1: Background composition, observed and expected yields, and limits at the 95% CL for all three-lepton channels combined tag selections for an integrated luminosity of  $19.5 \text{ fb}^{-1}$ . The uncertainties in the background estimation include the statistical and systematic components separately (in that order).

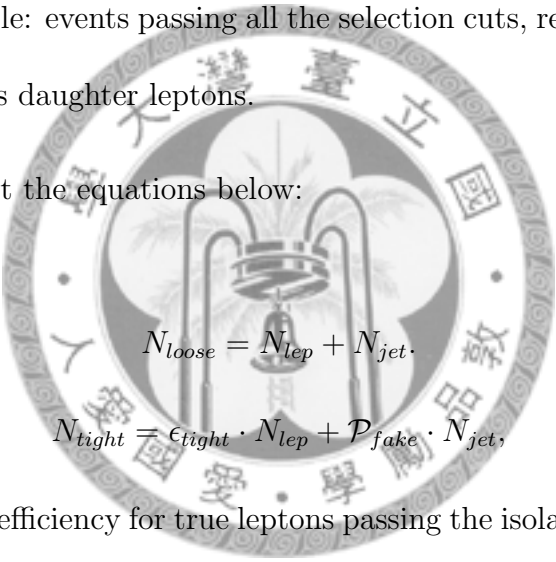
# Appendix A: Lepton Isolation Method

This matrix method can be used to estimate the background process with two true leptons, which are the  $Z + \text{jets}$  and  $t\bar{t}$  processes, we call it as  $N_{2l}$ . For other processes we call it  $N_{3l}$ . After the  $Z$  selection, we will look at the third lepton where in  $N_{2l}$  we consider the third one to be faked by a jet.

We define the following two samples:

- Tight-cut sample: events passing all the signal extraction cuts;
- Loose-cut sample: events passing all the selection cuts, regardless the isolation cuts on the  $W$ 's daughter leptons.

Then we construct the equations below:



$$N_{loose} = N_{lep} + N_{jet}.$$

$$N_{tight} = \epsilon_{tight} \cdot N_{lep} + \mathcal{P}_{fake} \cdot N_{jet},$$

where  $\epsilon_{tight}$  is the efficiency for true leptons passing the isolation cuts and  $\mathcal{P}_{fake}$  is the corresponding ‘efficiency’ of fake leptons. We will obtain  $\epsilon_{tight}$  and  $\mathcal{P}_{fake}$  directly from data.

The efficiency for the true leptons to pass the isolation cuts can be estimated with the ‘tag-and-probe’ method. An independent  $Z$ -enriched sample is used by requiring two opposite-charged leptons with the same flavor, with the invariant mass within the 60 – 120 GeV range. The leptons are required to have  $p_T > 20\text{GeV}$  and pass the above lepton ID selections. Only one  $Z$  candidate per event is allowed in the above mass window. The efficiency is then obtained via the following equation:

$$\epsilon_{tight} = \frac{2(N_{TT} - B_{TT})}{(N_{TF} - B_{TF}) + 2(N_{TT} - B_{TT})}.$$



Here  $N$  is the total number of events in the  $Z$ -candidate mass window, while  $B$  is combinatorial background from  $W$  events, as estimated from a linear fit on events outside of the  $Z$  mass window. The sub-note  $TT$  means that both leptons pass the isolation cuts and  $TF$  means that one of the leptons fails the isolation cuts in which does not include those of  $TT$ .

Fake leptons in the samples would be mostly coming from jets fragments which has poorer isolation. We estimate the ‘efficiency’ that a fake lepton passing the loose and tight isolation requirement by looking into a multi-jet sample. Events with two prompt jets having good back-to-back behavior,  $\Delta\phi(jet_1, jet_2)$  with only one lepton candidate in an event is chosen. The MET of the event is required to be less than 30 GeV to reject  $W$  contribution. The isolation efficiency is obtained by taken the ratio of pt distributions that passing tight over loose isolation requirement and fitted with a linear function.

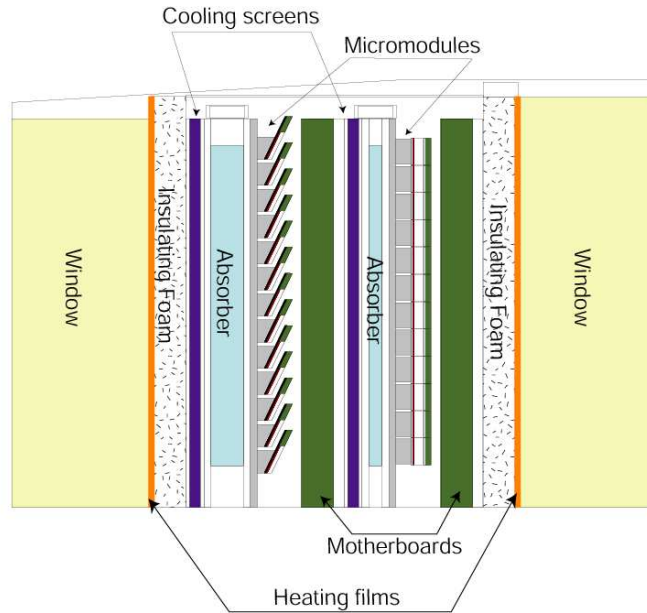
With the isolation efficiencies for true and fake leptons determined as described above, we can estimate the  $ll + X$  and  $WZ + X$  from the total number of events in the two samples after  $WZ$  plus two jets requirement. From the relative yields of the two processes and their acceptance of top mass requirement as well as the b-tagging efficiencies of data, the estimated yields in full selection are  $0.10 \pm 0.02 \pm 0.02$  and  $0.33 \pm 0.10 \pm 0.06$  for Drell–Yan and  $t\bar{t}$ , respectively. This is consistent with the yield of MC estimation.

## Appendix B: Preshower Full Depletion Voltage Measurement

The endcap preshower, short as ES, is a sub-unit of the electrocalorimeter. It is located at the endcap right in front of the endcap electrocalorimeter (see figure 2.5). Since there are two sides for endcap, we label the two set of sensors by ES+ and ES-. The major goal of ES is to discriminate the photon of Higgs decay from the photon of pion decay. The photon from pion decay is actually two photons but of small deviation, so it should be discernible using detectors of good spatial resolution.

The main components of ES is the absorber and the sensors. The absorber is made of lead which initiate the electromagnetic shower. When the collision occur, photons and electrons will hit the absorber and start showering. The resulting positrons and electrons will then leave signals on the silicon sensors. There are two absorbers, in the front is one of  $2X_0$  (radiation length), and in the rear is of  $X_0$ . These two absorbers are followed by the silicon sensors with the effective spatial resolution of  $61 \times 61 \text{ mm}^2$ . We name these four sets of sensors by their location as ES+front, ES+rear, ES-front and ES-rear.

The reverse bias voltage ( $V_r$ ) applied on the silicon sensor creates an electric field which drives the electrons and holes created by the passing high energy particles to the electrodes for signal collection. The signal grows and the noise decreases with the electric field. However, the maximum electric field is limited by the design of the sensors. When the electric field reaches its maximum, we call the corresponding voltage as the full depletion voltage, the  $V_{fd}$ . When reaches  $V_{fd}$ , it is of no use to further increase the voltage, and the over setting of the voltage may leads to higher



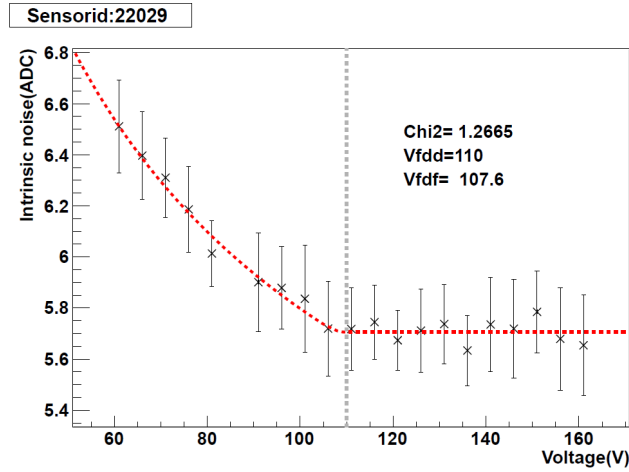
The one-side view of preshower sensor, the interaction point is to the left of this figure. When the collision occur, photons and electrons will hit the absorber (blue) and start showering. The resulting positrons and electrons will then leave signals on the silicon sensors (green and grey).

leaking current or even the breakdown of the sensors.

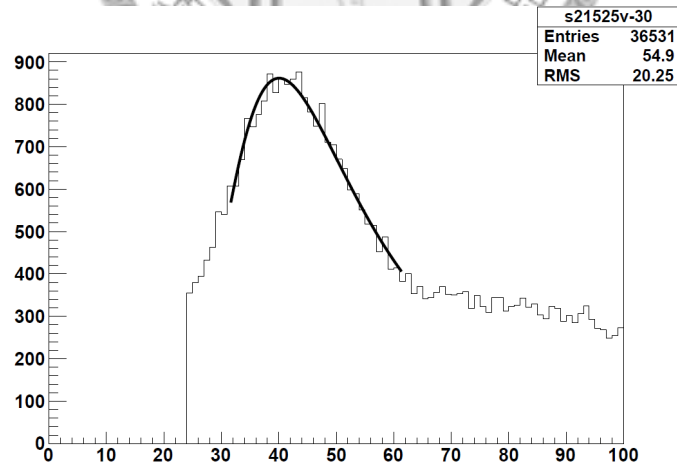
There are 4288 different sensors in total and each of them are of different Vfd. The Vfd will also change due to the radiation damage. We calculate the Vfd by measuring the signal (noise) to  $V_r$  relation, and we take the  $V_r$  to be Vfd at the point the signal (noise) reaches its maximum (minimum). The measurements are carried out in different time for the determination of the radiation effect.

The signal collected by the sensors is a landau distribution and its peak is called the most probable value (MPV) of the signal collection. The signal we refer to when we say 'the signal grows with  $V_r$ ,' is actually referring the the MPV of the signal.

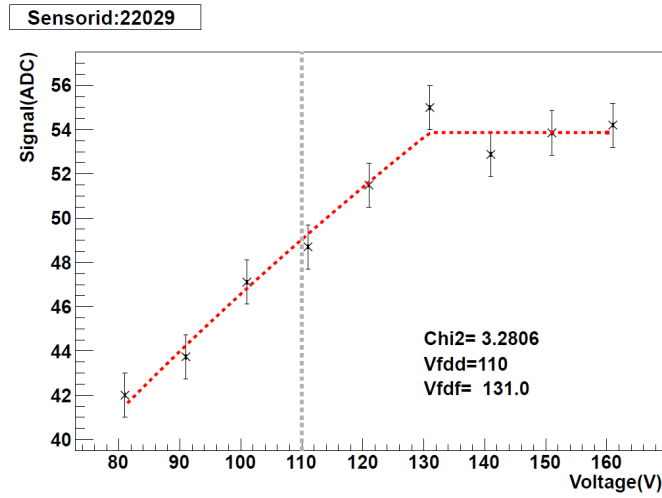
The signal to  $V_r$  behavior is then used to extract the Vfd. We measure the Vfd in this manner in 2010 and 2012, and we observed a Vfd drop as was expected.



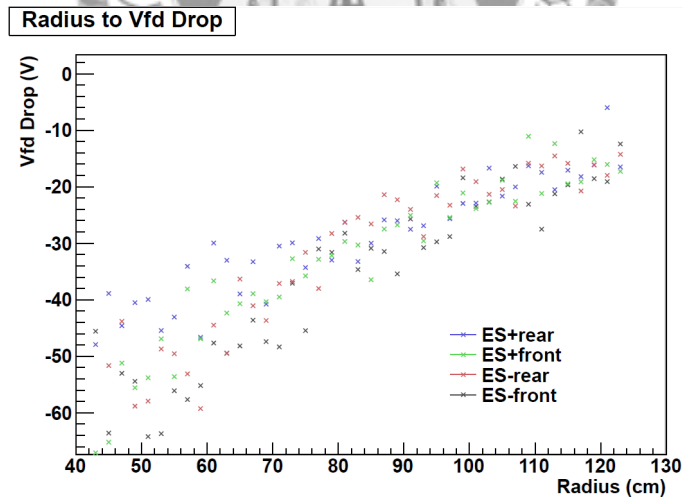
The noise to Vr behavior of one of the 4288 sensors recorded in early 2010 when there were no proton collision occurring. We expect the radiation damage to be minimum at the time of this measurement. The noise reaches its minimum at the voltage 107.6. We compare the value with the one measured when it was first installed and confirmed the measurement is reasonable. The fitting curve is  $1/\sqrt{x}$  in the left and constant in the right.



The signal distribution of a certain sensor at certain voltage recorded using collisions in 2010, the left edge is cut off due to the threshold setting. We fit the peak region to extract the value of MPV.



The signal to Vr behavior of one of the 4288 sensors recorded in middle 2010 when the collision occurring. The signal reaches its maximum at the voltage 131.0. The fitting curve is a straight line in the left and constant in the right.



The Vfd drop from measurement during the 2010 data-taking to 2012 data-taking is plotted as a function of the radial distance from the center, the Vfd drop of sensors having the same radius being averaged. The Vfd drop in the center is more severe, which is the consequence of stronger radiation.

The measured full depletion voltage of some sensors.

ID	Radius (cm)	Measured Vfd (2010)	Measured Vfd (2012)	Measured Vfd Drop
22029	52.0974	131.0	92.1	-38.9
22129	52.0858	144.5	95.5	-49.0
22028	46.011	132.6	73.6	-59.0
22128	45.9979	127.0	84.4	-42.7
22031	64.278	131.0	92.7	-38.3
22131	64.2686	128.8	104.6	-24.2
22030	58.1867	131.0	84.0	-47.0
22130	58.1763	131.0	123.7	-7.3
22033	76.4647	128.8	96.7	-32.1
22133	76.4568	131.0	103.2	-27.8
22032	70.3708	121.6	92.9	-28.8
22132	70.3622	128.2	92.7	-35.5
22035	88.6552	131.0	91.6	-39.4
22135	88.6483	131.0	97.0	-34.0
22134	82.5523	131.0	102.1	-28.9
22036	94.7513	148.6	122.7	-25.9
22136	94.7449	120.8	107.0	-13.8
22038	106.945	135.2	107.5	-27.7

# Bibliography

- [1] S.L. Glashow, J. Iliopoulos, L. Maiani, 1970.
- [2] J. A. Aguilar-Saavedra and B. M. Nobre, Phys. Lett. B 553, 2003.
- [3] D. Atwood, L. Reina and A. Soni, Phys. Rev. D 55, 1997.
- [4] H. J. He and C. P. Yuan, Phys. Rev. Lett. 83, 1999.
- [5] CMS Physics TDR: Volume I (PTDR1), Detector Performance and Software, 2007.
- [6] Johan Alwall, Michel Herquet, Fabio Maltoni, Olivier Mattelaer, Tim Stelzer, 2011.
- [7] P. de Causmaecker, R. Gastmaex, W. Troost, and T.T. Wu, Phys. Lett. 105B, 215, 1981.
- [8] hep-ph/0603175, LU TP 06-13, FERMILAB-PUB-06-052-CD-T, 2006.
- [9] arXiv:1101.1652, TAUOLA for simulation of tau decay and production, 2011.
- [10] Z. Was, TAUOLA the library for tau lepton decay, and KKMC / KORALB / KORALZ / ... status report, Nucl.Phys.Proc.Suppl. 98 (2001) 96 V102, doi:10.1016/S0920-5632(01)01200-2, arXiv:hep-ph/0011305.

- [11] Maryam Zeinali, Measurement of the Jet Energy Scale in the CMS experiment with the First LHC Proton Collisions, 2011
- [12] J. A. Aguilar-Saavedra, Top flavor changing neutral coupling signals at a linear collider, Phys. Lett. B 502 (2001) 115, doi:10.1016/S0370-2693(01)00162-9, arXiv:hep-ph/0012305.
- [13] G. Lu et al., Rare top quark decays  $t$  to  $cV$  in the topcolor assisted technicolor model, Phys. Rev. D 68 (2003) 015002, doi:10.1103/PhysRevD.68.015002, arXiv:hep-ph/0303122.
- [14] ATLAS Collaboration, A search for flavour changing neutral currents in top-quark decays in pp collision data collected with the ATLAS detector at  $\sqrt{s} = 7$  TeV. JHEP 1209 (2012) 139, doi:10.1007/JHEP09(2012)139, arXiv:1206.0257.
- [15] CMS Collaboration, The CMS experiment at the CERN LHC, JINST 03 (2008) S08004, doi:10.1088/1748-0221/3/08/S08004.
- [16] T. Han and J. L. Hewett, Top charm associated production in high-energy  $e+e$  collisions, Phys.Rev. D60 (1999) 074015, doi:10.1103/PhysRevD.60.074015, arXiv:hep-ph/9811237.
- [17] CMS Collaboration, Performance of b-jet identification in CMS, CMS Physics Analysis Summary CMS-PAS-BTV-11-001, (2011).
- [18] Bernardo, Jose M.; Smith, Adrian F. M. (1994). Bayesian Theory. Wiley. ISBN 0-471-49464-X.